NASA Contractor Report CR-205409

Evaluation of the 29-km Eta Model for Weather Support to the United States Space Program

Prepared By:
Applied Meteorology Unit

Prepared for:
Kennedy Space Center
Under Contract NAS10-96018

NASA
National Aeronautics and
Space Administration

Office of Management

Scientific and Technical
Information Program

1997

Attributes and Acknowledgments

NASA/KSC POC:
Dr. Francis J. Merceret
PH-B3

Applied Meteorology Unit (AMU)

John Manobianco
Paul Nutter

Table of Contents

Table of Contents
(continued)

Table of Contents
(continued)

List of Figures

List of Figures
(continued)

List of Figures
(continued)

List of Tables

List of Tables
(continued)

Executive Summary

This purpose of this report is to document the Applied Meteorology Unit's (AMU) evaluation of the National Centers for Environmental Prediction (NCEP) 29-km eta model. NCEP started running the 29-km version of the eta (meso-eta) model in August 1995 and they continue to update the model configuration, initialization, and physical parameterizations. The objective of the evaluation is to assess the utility of the meso-eta model for local weather forecasting in support of 45th Weather Squadron (45WS), Spaceflight Meteorology Group (SMG), and National Weather Service (NWS) Melbourne (MLB) operational requirements.

The evaluation protocol was determined by a technical group comprised of meteorologists and forecasters from 45WS, SMG, NWS MLB, and AMU. The evaluation protocol consisted of both objective and subjective components. The objective verification of the meso-eta model focused on the overall accuracy of wind, temperature, and moisture forecasts at selected stations. The statistical measures used to quantify model forecast errors were the bias, root mean square (RMS) error, standard deviation, and consistency. Using these statistics, point forecasts from the meso-eta model were verified against standard surface and upper air observations. The subjective evaluation includes warm-season forecast exercises and phenomenological verification focusing primarily on limited case studies and seasonal evaluations of sea breezes, thunderstorms, and cold fronts. Subjective verification is performed using gridded data only from 0300 UTC model runs.

Objective verification results generally indicate that meso-eta model point forecasts at selected stations exhibit minimal error growth in terms of RMS errors, and except for a few parameters, are reasonably unbiased. However, there are some exceptions identified in this evaluation as indicated by the following list of model biases.

- 2-m dew point temperatures and 10-m wind speeds are typically overestimated at Cape Canaveral Air Station, FL (XMR) during the cool season.
- Diurnal changes exist in the average forecast errors for 2-m temperature, 10-m wind speed and MSLP at Edwards Air Force Base, CA (EDW).
- At XMR and Tampa Bay, FL (TBW), warm (cool) season forecast soundings are typically drier and more stable (unstable) than observed.
- The height of the lower tropospheric inversion at XMR and TBW is misrepresented during the cool season.
- Tropopause heights are misrepresented by the model at all three stations.

Results from the objective verification do not indicate whether the model is more accurate overall during either the warm or cool season. However, results from the subjective verification suggest that the model forecasts over central Florida may be more useful during the cool season. This statement is based on the fact that the meso-eta model resolution is not yet sufficient to resolve the small-scale details of sea and river/lake breeze circulations, thunderstorm outflow boundaries, and other phenomena which play a dominant role in determining the short-term evolution of weather over east central Florida during the warm season.

Objective verification results also demonstrate that forecasts of selected parameters are reliable over the course of an entire season. On the other hand, results from the subjective verification demonstrate that model forecasts of developing weather events such as thunderstorms, sea breezes, cold fronts, etc. are not always as accurate as implied by the seasonal error statistics. The subjective

verification is indeed very important to quantify added value of model forecasts for these specific phenomena which can not be readily inferred from statistics over many cases (i.e. from objective verification). Some results from the subjective evaluation which can be important for operational forecast concerns include the following.

- Sea-breeze case studies reveal that the model generates a dynamically-consistent thermally direct circulation over the Florida peninsula, although at a larger scale than observed. Seasonal verification of sea breezes indicates that the model forecasts the occurrence of east and/or west coast sea breezes roughly 50% of the time they are observed.

- Thunderstorm verification reveals that the meso-eta model is capable of predicting areas of organized convection, particularly during the late afternoon hours. On the other hand, the model is also subject to subtle errors that can lead to incorrect forecasts of warm season convective precipitation. In particular, the model often generates excessive rainfall during the morning hours and is not capable of accurately forecasting individual thunderstorms.

- Verification of cold fronts during the cool season reveals that the model is capable of forecasting a majority of cold frontal passages through east central Florida to within ±1-h of observed frontal passage.

Warm season forecast exercises demonstrate that animation of 3-h model output with color enhancements and overlay of multiple fields is helpful to identify features and trends that could become important for developing weather. Availability of digital gridded model output at 3-h intervals is important because it gives users the flexibility in display and analysis options while providing the temporal resolution needed to track specific aspects of forecast weather events such as the timing of cold frontal passages. In order to exploit the four-dimensional capability of the meso-eta and other models in forecasting possible realizations of the atmosphere, sufficient communication bandwidth and computer processing power are necessary to retrieve, process, and examine output data. This requirement will become more important in the future as NCEP increases the number of meso-eta model runs per day, the model resolution, and potentially the frequency of model output.

The evaluation methodology used in this study enables an assessment of both forecast accuracy and utility for model users. However, the short 4-month evaluation periods impose limitations on the completeness of the verification, particularly with regard to sample sizes. Subjective verifications in this evaluation are limited to simple case studies in order to examine a greater number of phenomenological features which impact 45WS, SMG, and NWS MLB operations. The case studies highlight some of the capabilities and limitations of the meso-eta model but are not designed to fully explore the cause(s) of model errors. Seasonal evaluations of sea breezes, thunderstorms, and cold fronts are designed to quantify how consistently the model provides utility in forecasts of these phenomena. However, more detailed examination of model capabilities and limitations is beyond the scope of the present evaluation given available AMU resources.

Ongoing changes to the model configuration, initialization, and physical parameterizations could modify some of the seasonal error characteristics identified by the AMU's objective verification of surface and upper air forecasts. In order to increase the sample size and track possible changes in model accuracy, the objective component of the meso-eta evaluation is being extended to include a second warm and cool season period from May through August 1997 and October 1997 through January 1998, respectively. A comparison between results from the 1996 and 1997 seasons will highlight any changes in the error characteristics at selected stations which may occur in response to

updates in the meso-eta model configuration. This analysis will also prove useful for model users since the 1997/1998 results will be more representative of the meso-eta model's current capabilities.

1.0 Introduction

1.1 Background

Weather support for ground and aerospace operations at the Kennedy Space Center (KSC) and Cape Canaveral Air Station (CCAS) requires accurate forecasts of winds, clouds, ceilings, fog, rain, lightning, and visibility. The National Aeronautics and Space Administration (NASA) and United States Air Force (USAF) funded private corporations to develop and deliver numerical weather prediction systems that are designed to run locally on high performance workstations. In general, the objective of installing and running local mesoscale modeling systems is to produce more precise and detailed short-range (< 24 h) forecasts than operational models such as the Nested Grid Model (NGM) and eta model run at the National Centers for Environmental Prediction (NCEP). Local modeling systems have the potential to provide added value for short-range forecasting because they typically incorporate local data, run at finer horizontal resolutions over smaller domains, and use more sophisticated physical parameterizations than national-scale, operational models.

The main components of the local mesoscale modeling systems developed for KSC/CCAS are the Mesoscale Atmospheric Simulation System (MASS) and Regional Atmospheric Modeling System (RAMS) models. The RAMS model is used in the Emergency Response Dose Assessment System (ERDAS) and the Parallelized RAMS WEather Simulation System (PROWESS). MASS is designed to provide forecasts of specific thunderstorm-related phenomena such as precipitation and high winds. ERDAS is designed for range safety to provide emergency response guidance for operations at KSC/CCAS in case of a hazardous material release or aborted vehicle launch. PROWESS is designed to forecast the development of site-specific thunderstorms over the KSC/CCAS work areas.

As part of their ongoing evaluation and technology transition plan, the Applied Meteorology Unit (AMU) performed detailed evaluations of MASS (Manobianco 1996) and ERDAS (Evans 1996). Because ERDAS has mesoscale modeling and diffusion capabilities that are far more advanced than current local models, it was found to provide significant added value for range safety personnel. Similar high resolution guidance designed specifically for KSC/CCAS safety applications is not routinely available from other operational centers. In response to its proven utility and operational need, ERDAS is currently being transitioned into KSC/CCAS safety operations as part of the replacement and upgrade of the Meteorological And Range Safety Support (MARSS) system. On the other hand, larger-scale forecasts of wind, temperature, precipitation, and other parameters for many areas including east-central Florida are routinely provided by the NCEP. Many components of the MASS evaluation indicated that it could not consistently produce more skillful short-range precipitation and wind forecasts than those already provided by the NCEP's NGM model.

When the AMU completed the MASS evaluation in December 1995, two subsequent teleconferences were convened with NASA Headquarters, NASA KSC, 45th Weather Squadron (45WS), Spaceflight Meteorology Group (SMG), and the National Weather Service (NWS) Melbourne (MLB) to review the evaluation results and discuss options for an out-of-cycle or "mid-course correction" to the AMU mesoscale modeling task. The following points were raised during these two teleconferences.

- It was evident from the evaluation that the current version of MASS did not provide sufficient added value over NCEP models to justify the cost of continuing the evaluation with the intent to transition MASS for operational use.

- Data deficiencies such as limited access to NCEP gridded data and no access to digital data from the WSR-88D at MLB and the KSC/CCAS network of five 915-

MHz Doppler Radar Wind Profilers (DRWP) probably limited the utility of local modeling systems such as MASS and PROWESS.

- NCEP started running a 29-km or mesoscale version of the eta model in August 1995 (Mesinger 1996) and plans to run a 10-km, non-hydrostatic version of the model over the entire United States by the year 2000 (Kalnay et al. 1996).

The first two points suggest that a number of issues need to be addressed before local modeling systems such as MASS and PROWESS could provide significant added value to justify their life-cycle costs. In addition, 45WS, SMG, and NWS MLB agreed that an evaluation of the 29-km or meso-eta model would likely result in a low-risk payoff within one year, namely that the AMU would be able to determine the utility of NCEP's best mesoscale model for local forecasting. Based on these points, 45WS, SMG, and NWS MLB reached a consensus to shift the AMU modeling task from evaluating local models to evaluating NCEP's operational mesoscale model. As a result of this "mid-course correction", the AMU was directed to terminate all work with MASS, delay any prioritized work on evaluating PROWESS, and begin evaluating the meso-eta model.

1.2 Applied Meteorology Unit Tasking

Under the Mesoscale Modeling Task (005), Subtask 2, the AMU evaluated the most effective ways to use NCEP's 29-km eta model to meet 45WS, SMG and NWS MLB requirements. The evaluation methodology was determined by a technical working group consisting of several meteorologists and forecasters from the AMU, 45WS, SMG, and NWS MLB. Based on recommendations from the technical working group, the AMU determined the data acquisition requirements, and designed and implemented the evaluation protocol.

1.3 Purpose and Organization of the Report

This purpose of this report is to document the AMU's evaluation of the 29-km eta model. Section 2 provides a brief overview of the eta model. The evaluation protocol is summarized in Section 3. Section 4 discusses results of the objective evaluation while Section 5 discusses results from the subjective evaluation. A summary and lessons learned from the overall evaluation are presented in Section 6. Finally, Section 7 highlights the AMU's future work on evaluating the 29-km eta model.

2.0 Eta Model Overview

The primary mesoscale modeling efforts at NCEP are focused on the development of the eta model (Rogers et al. 1995). The eta model takes its name from a vertical coordinate that is a generalization of the terrain-following sigma coordinate. However, the eta coordinate is normalized by sea-level pressure rather than surface pressure so the resulting eta surfaces are quasi-horizontal. This feature of the eta coordinate system eliminates errors in pressure gradient terms computed over steeply sloping terrain and also produces model orography in the form of discrete blocks or steps (Mesinger and Black 1992).

The original version of the eta model with a horizontal resolution of 80 km and 38 vertical layers replaced the Limited-Area Fine Mesh model in June 1993 (Black 1994). In October 1995, NCEP increased the horizontal resolution of the operational "early" eta model from 80 km to 48 km. The term "early" refers to the fact that the 48-km eta model run begins 1.25 h after the data cutoff time to provide forecast guidance as quickly as possible (Mesinger 1996). Since August 1995, NCEP has also been running a mesoscale version of the eta model with a horizontal resolution of 29 km and 50 vertical layers (Mesinger 1996). The 29-km or meso-eta model is started after the 48-km model run has completed.

The relevant numerics and physics of the eta model are summarized in Table 2.1. The specific details regarding the dynamics, physics, horizontal domain, initialization, and other aspects of the eta model configuration are provided by Black (1994) and Rogers et al. (1995, 1996). Following upgrades to the 48-km version in January 1996, the "early" and meso-eta model configurations are now identical except for resolution and data assimilation. The Eta Data Assimilation System (EDAS) for the "early" eta consists of four 3-h analysis-forecast cycles that incorporate high frequency observations such as aircraft and profiler data (Rogers et al. 1996). The meso-eta is also intialized with the EDAS but it runs for one 3-h analysis-forecast cycle from 0000-0300 UTC or 1200-1500 UTC. The EDAS is currently started with a first guess from the Global Data Assimilation System (GDAS). In the near future, NCEP plans to restructure the EDAS so that it uses the previous EDAS cycle rather than the GDAS to provide a first guess for subsequent analyses.

Table 2.1. Eta model attributes*.

Dynamics
Model top = 25 mb
Time step = 72 s
Semi-staggered Arakawa E-grid
Gravity wave coupling scheme
Silhouette-mean orography
Split-explicit time differencing
Physics
Explicit grid-scale cloud and precipitation
Modified Betts-Miller convective adjustment
Mellor-Yamada (2.5) for free atmosphere vertical turbulent exchange Mellor-Yamada (2.0) near ground
Geophysical Fluid Dynamics Laboratory radiation scheme
Viscous sublayer over water

*from Black (1994) and Rogers et al. (1996)

3.0 Evaluation Protocol

The evaluation protocol was determined by a technical group consisting of several meteorologists and forecasters from 45WS, SMG, NWS MLB, and the AMU. The technical working group held three teleconferences that resulted in an evaluation strategy consisting of both objective and subjective components. The objective verification of the eta model focuses on the overall accuracy of wind, temperature, and moisture forecasts at selected stations. The subjective or phenomenological verification assesses the eta model's capabilities in forecasting convective activity, the location and movement of fronts and the onset, depth, and propagation of sea-breezes. All of these parameters are important in evaluating launch commit criteria (LCC) for manned and unmanned vehicle launches and flight rules (FR) for Shuttle landings. The following sections summarize how the AMU is currently accessing the 29-km eta model forecasts and provide specifics of the objective and subjective evaluation criteria designed by the technical working group.

3.1 Data Acquisition

The 29-km eta data are obtained via the Internet from NOAA's Information Center (NIC) FTP server. The gridded data from the 0300 UTC cycle of the meso-eta are downloaded at approximately 0900 UTC. (Note the gridded data from the 1500 UTC cycle of the eta model are not being used for the evaluation discussed here.) NCEP interpolates the 29-km eta model output to the Advanced Weather Interactive Processing System (AWIPS) 40-km grid at 3-h intervals for the entire meso-eta 33-h forecast period. After the meso-eta data on the AWIPS grid are retrieved from the NIC, a subset of the data are decoded from GRIdded Binary (GRIB) format using software contained in the GEneral Meteorological PAcKage (GEMPAK; desJardins et al. 1997). In addition to gridded data, the point forecasts at selected stations are downloaded from both the 0300 UTC and 1500 UTC cycles of the meso-eta model. These files contain surface and upper air parameters at 1-h intervals and are decoded from Binary Universal Form for the Representation of meteorological data (BUFR) using GEMPAK software.

3.2 Objective Evaluation Criteria

The objective verification of the 29-km eta model examines forecast errors for the parameters shown in Table 3.1. The station or point forecasts from the 0300 UTC and 1500 UTC meso-eta model cycles are verified against standard surface and rawinsonde observations. Hourly surface observations are taken at the Shuttle Landing Facility, FL (TTS), Edwards Air Force Base, CA (EDW), and Tampa International Airport, FL (TPA). Rawinsonde observations are taken twice daily at EDW, CCAS (XMR), and Tampa Bay (TBW). The XMR and EDW stations are selected because they are the primary and secondary landing sites for the Shuttle. The TBW site is chosen to compare model errors at two coastal stations on the eastern (XMR) and western (TBW) edge of the Florida peninsula. Station forecasts are extracted from the meso-eta model grid point nearest to the rawinsonde observation sites. Although surface and rawinsonde observations are not co-located at XMR and TBW, the available sites are separated by not more than about 30 km (i.e. the meso-eta model grid spacing). In order to avoid confusion, all subsequent references to rawinsonde and surface verification will use the rawinsonde station identifiers (XMR, TBW, EDW).

Hourly surface observations are used to verify 0- to 33-h forecasts of mean sea-level pressure, 2-m temperature (T) and dew point temperature (T_d), and 10-m winds (u, v). Upper air winds (u, v), temperature (T), moisture (q), and height (z) are verified at 25-mb intervals from 1000 to 50 mb and at selected height levels from 1000 to 70000 ft. Log-linear interpolation of data is used between available pressure levels while straight linear interpolation is used between available height levels. At XMR and EDW, rawinsondes are usually released at 0900 (1000) UTC and 2100 (2200) UTC during

daylight savings (standard) time. However, variations in the release time do occur so three verification periods are defined according to the schematic illustrated in Fig. 3.1. Periods 1, 2, and 3 range from 5-10 h, 17-22 h, and 29-33 h into the forecast cycle, respectively. Although rawinsonde release times may vary at XMR and EDW, forecast verification at all stations always coincides with the observation time. At TBW, forecast verification occurs at 0000 and 1200 UTC.

Table 3.1. Meso-eta objective verification parameters.

Parameter	Levels
Mean sea-level pressure	--
u, v	10 m
T, T_d	2 m
u, v, T, q, z	selected*
Precipitable water (PWAT; mm)	--
Convective available potential energy (CAPE; J kg^{-1})	--
Convective inhibition (CINS; J kg^{-1})	--
Lifted index (LIFT; °)	--
K index (KINX)	--
Ground relative helicity (HLCY; m^2 s^{-2})	0-3 km
Microburst day potential index (MDPI)	--
Thickness	1000-850 mb
Mean layer wind	850-500 mb
Mean layer relative humidity	850-500 mb

*refer to text for description

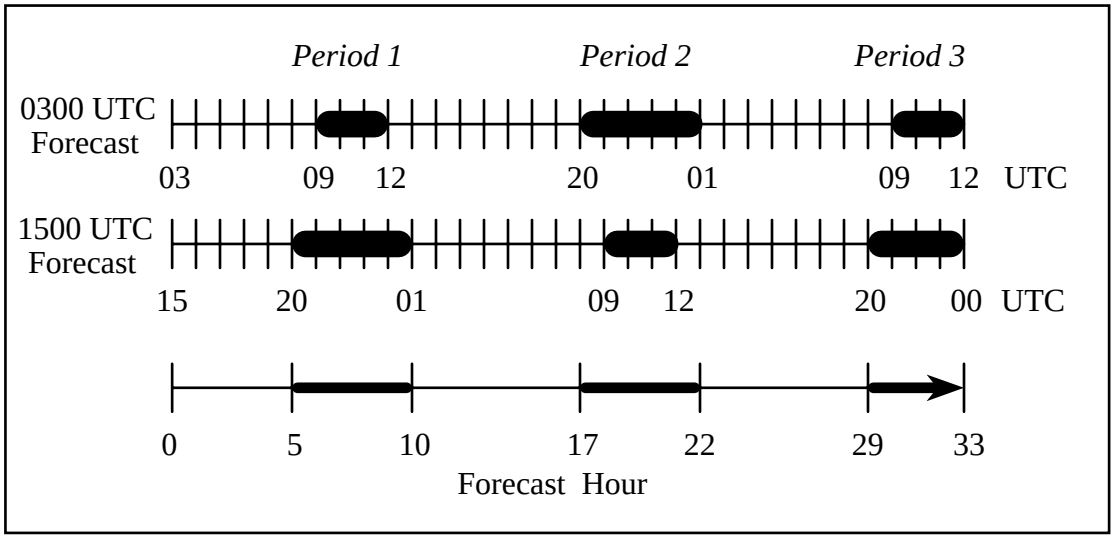

Figure 3.1. Definition of available windows for objective verification of upper air forecasts.

The parameters such as precipitable water, mean layer wind and relative humidity, and stability indices are included because they can be used to assess the potential for convective activity. Except for helicity (Davies-Jones et al. 1990; Lilly 1986) and Microburst Day Potential Index (MDPI; Wheeler and Roeder 1996), stability indices are derived using routines in GEMPAK. Since convection is usually not a forecasting concern at EDW, stability indices are not presented for that station. Winds

are verified in terms of speed and direction since these quantities are more familiar to model users than zonal (u) and meridional (v) wind components. Except for the 10-m winds, the meso-eta model forecasts are not benchmarked against other models, climatology, or persistence. For 10-m winds, model forecasts are compared with persistence for a period of 1 to 6 h.

The objective verification considers 29-km eta model forecasts from May through August 1996 (warm season) and from October 1996 through January 1997 (cool season). Within each seasonal evaluation period, the original evaluation protocol specified that verification would be stratified by average wind direction in the layer from 950 to 600 mb using seven wind regimes following Holle et al. (1992). This type of stratification is designed to determine if the model forecast errors are sensitive to specific flow regimes which are defined by layer-averaged wind directions. However, there are a limited number of available forecast/observation pairs in each of the seven wind regimes during the four-month warm or cool season. These small sample sizes make it difficult to draw meaningful conclusions regarding error characteristics as a function of flow regime (Panofsky and Brier 1958). Instead, westerly and easterly regimes are defined based on winds that are approximately perpendicular to Florida's east coast. In particular, the 950- to 600-mb layer-averaged winds are considered westerly between 158˚ and 338˚ and easterly outside that range. Typical sample sizes for surface and upper air forecast/observation pairs for each station and wind regime are listed in Table 3.2.

Table 3.2. Typical seasonal sample sizes for valid pairs of forecast/observed point data. The actual sample sizes vary for any given verification time, vertical level, and parameter but are on the order of the numbers shown here. "West" and "East" represent sample sizes after stratification by the 950- to 600-mb layer-averaged wind direction while "All" represents the size of combined data sets (see text). Only data from 0300 UTC forecasts/observations are included in the surface data sets (see section 4.1). Upper air samples use all available data from both 0300 and 1500 UTC forecasts/observations.

		XMR		TBW		EDW	
		Warm	Cool	Warm	Cool	Warm	Cool
Surface Data	All	70	70	75	95	75	70
	West	25	45	30	45	75	40
	East	45	25	45	30	0	30
Upper Air Data	All	130	125	145	145	75	55
	West	65	90	70	100	65	40
	East	65	35	75	45	10	15

The statistical measures used here to quantify model forecast errors are the bias, root mean square (RMS) error, standard deviation, and consistency. If Φ represents any of the variables in Table 3.1, then forecast error is defined as $\Phi' = \Phi_f - \Phi_o$ where the subscripts f and o denote forecast and observed quantities, respectively. In cases where the magnitude of the wind direction error exceeds 180˚, the error is recomputed by first subtracting 360˚ from the larger of the forecast or observed wind direction. The bias is computed as

$$\text{bias (p, t)} = \overline{\Phi'} = \frac{1}{N}\sum_{i=1}^{N}\Phi' \qquad (1),$$

the RMSE is computed as

$$\text{RMSE (p, t)} = [\text{MSE}]^{1/2} = \left[\frac{1}{N}\sum_{i=1}^{N}(\Phi')^2\right]^{1/2} \qquad (2),$$

and the standard deviation of the errors is computed as

$$\sigma'(p,t) = \left[\frac{1}{N-1} \sum_{i=1}^{N} (\Phi' - \overline{\Phi}')^2 \right]^{1/2} \quad (3).$$

When N is used rather than N-1 in Equation (3), Murphy (1988) demonstrated that the following decomposition could be applied to the MSE:

$$\text{MSE} = \overline{\Phi}'^2 + \sigma'^2 \quad (4).$$

Therefore, the total model error consists of contributions from model biases ($\overline{\Phi}'^2$) and random variations in the forecast or observed data (σ'^2). Note that if the model bias or systematic error is small, most of the MSE is due to random, non-systematic type variability. In fact, it is possible that a very small contribution to the non-systematic error could result simply from different reporting precision between the model forecasts and observations.

In addition to these standard forecast verification methods, a fourth parameter is defined in an attempt to provide users with a measure of confidence in forecast stability. Following Leslie et al. (1994), model forecast consistency is computed at a point to measure the bias between subsequent forecasts verifying at the same time but initialized 12-h apart. If Θ represents any of the parameters from the 0300 UTC or 1500 UTC forecast cycles listed in Table 3.1, then consistency is defined as

$$\text{Consistency}(p,t)_{[03,15]} = \frac{1}{N-1} \sum_{i=1}^{N-1} \left[\Theta_{[03,15]}(i, t+12) - \Theta_{[15,03]}(i+1, t) \right] \quad (5).$$

The subscript i in Equations (1) through (5) refers to an individual model forecast and N is the total number of point forecasts initialized at 0300 UTC and 1500 UTC. As with the forecast bias (Eq. 1) model consistency is either positive or negative. Other non-standard measures which are independent of sign are defined by Leslie et al. (1994) but are not used in this study. On average, small values of consistency indicate that only minor differences occur between model runs. Conversely, larger values indicate that subsequent model runs tend to disagree with one another.

Each of the statistics above are a function of pressure (p) and time (t). For quality control, gross errors in the data are screened manually and corrected, if possible. Individual errors which are greater than two standard deviations from the mean error (bias) are removed. Although this procedure removes approximately 5% of the data, it is very useful in objectively flagging bad data points.

3.3 Subjective Evaluation Criteria

The subjective component of the meso-eta model evaluation consists of daily, real-time warm season forecast exercises by AMU personnel and very limited analyses of selected case studies from both warm and cool seasons. GEMPAK/ntrans software is used on a daily basis to generate graphics and view animated loops of 3-hourly meso-eta model output. In this manner, forecast variables such as wind, moisture, stability indices, convergence, helicity, etc. are displayed using time series plots, vertical cross sections, horizontal sections, and time-height sections. At the end of each day, the AMU archived gridded forecasts of these variables from the 0300 UTC runs of the meso-eta model. Point forecasts were also collected from the 0300 UTC and 1500 UTC model runs at XMR, TBW, EDW, and offshore buoy locations. In addition to the meso-eta forecasts, observational data were archived daily in order to perform the case study analyses. These data include surface, rawinsonde, 50-MHz and 915-MHz profiler, and Geostationary Operational Environmental Satellite (GOES-8)

visible and infrared (IR) satellite data. Other data such as KSC/CCAS mesonet towers, WSR-88D radar, and cloud observations from launch reconnaissance aircraft are available to verify these phenomenon.

The AMU daily weather forecast discussion was held during the warm season evaluation period (May through August 1996) on Monday through Friday at approximately 1330 UTC. In part, this component of the subjective evaluation was designed to simulate how operational forecasters may use the 0300 UTC cycle of meso-eta model to assist in forecasting the onset, depth, and motion of the east and/or west coast sea breeze, the occurrence and severity of convection within 25 miles of XMR, and the occurrence of steady state winds in excess of 18 kt at XMR over the subsequent 12 to 24 h. These phenomenon are being evaluated due to their primary importance for evaluation of LCC, Shuttle FR, and because severe weather associated with thunderstorms can be hazardous to equipment and personnel performing ground operations at KSC/CCAS. One member of the AMU staff lead the weather briefing and filled out a daily evaluation worksheet. The worksheet was used to record the availability of meso-eta data, note the occurrence and movement of east and/or west coast sea breezes and thunderstorms, log periods when wind speeds exceed 18 kt, and identify days suitable for case studies. The data from the Melbourne WSR-88D radar, geostationary satellites (GOES-8), KSC 50-MHz profiler, and KSC/CCAS mesonet towers are available in real time to help verify the specific phenomenon of interest.

The case studies are designed to focus on propagation and intensity of tropical waves, cloud ceilings and thickness, propagation of cold fronts, and mesoscale wind features identified from time-height sections of 50-MHz or 915-MHz profiler data that are not resolved by 12-h rawinsonde observations. The analyses of mesoscale wind features include cases from the warm and cool season while the analyses of clouds and cold fronts (tropical waves) are limited to cases from the cool (warm) season only. The cases are selected based on the occurrence or existence of tropical waves and cold fronts that are within 500-1000 km of KSC/CCAS or for challenging forecasts such as the development of stratocumulus clouds that occurs frequently in the cool season following the passage of a cold front. The analyses for each case study are limited so that a number of cases can potentially be examined to quantify the added value (if any) provided by the 29-km eta model in forecasting the aforementioned aspects of tropical waves, clouds, cold fronts, and strong winds.

3.4 Pre-Final Report Discussions

At the request of the AMU Chief, AMU personnel conducted informal discussions/briefings with SMG, 45WS, and NWS MLB to review results of the meso-eta evaluation prior to outlining and writing this final report. Note that these briefings were not part of the original evaluation protocol designed by the technical working group. The discussions were designed to (1) provide a status of the year-long AMU evaluation of the 29-km eta model, (2) solicit feedback from each group, and (3) determine what aspects of the evaluation results are most operationally useful based on prioritization by SMG, 45WS, and NWS MLB. These discussions were very informative and every attempt is made to incorporate as many of the suggestions and requests in this report which are consistent with the original model evaluation protocol.

4.0 Objective Evaluation Results

The results presented in this section focus on the objective verification of meso-eta point forecasts for XMR, TBW, and EDW as described in section 3.2. Objective verification of point forecasts provides a stringent test of model capabilities. Station observations sample many temporal and spatial scales of atmospheric phenomena, some of which cannot be resolved by the model. As a result, point verification should benefit higher resolution models which resolve finer scales of motion but it does tend to give a more pessimistic view of model performance than gridded verification. Nevertheless, point verifications are of more interest to end users of model guidance since, ultimately, forecasters want to understand characteristic strengths and weaknesses in model forecasts at specific locations.

Results of surface, upper air, and convective parameter verifications are presented in sections 4.1, 4.2, and 4.3, respectively. Examination of results for every parameter indicates that error characteristics are qualitatively similar under both westerly and easterly wind regimes. For example, positive and negative biases appear with similar magnitudes at approximately the same time and height. For this reason, all available data are combined and results shown below are not stratified by wind regime. Attempts to identify statistically significant differences between sample means at each station are not performed because sample sizes are rather small and because such efforts are beyond the scope of the current evaluation. Speculations about the source of model errors are provided where appropriate but should only be viewed as possibilities which are consistent with the statistical results.

4.1 Surface Forecasts

Examination of biases, RMS errors, and standard deviations for all the surface parameters outlined in section 3.2 indicates that diurnal fluctuations exist in the time series. That is, positive or negative biases occur at approximately the same time of day in either the 0300 or 1500 UTC forecast cycle. Since statistics from the 1500 UTC cycle provide little additional information, only statistics from the 0300 UTC forecast cycles are shown in the following sub-sections. In order to facilitate comparison, warm and cool season results for surface parameters are presented side by side in Figs. 4.1 through 4.11. Forecast consistency of surface parameters exhibits a different behavior and is considered below in section 4.1.8.

4.1.1 2-m Temperature

Surface 2-m temperature biases at XMR and TBW generally range within ±2 ˚C during both warm and cool seasons (Figs. 4.1a, b). Forecast temperatures at EDW are on average colder than observed, with biases reaching about –5 ˚C. In conjunction with these larger negative biases at EDW, RMS errors reach nearly 6 ˚C and are also larger than the RMS errors at XMR and TBW (Figs. 4.1c, d). As discussed in section 3.2 (Eq. 4), the bias and standard deviation represent systematic and non-systematic model errors which both make contributions to the total RMS error. In fact, except for the early part of the cool season forecasts, standard deviations at EDW are comparable in magnitude to those at XMR and TBW (Figs. 4.1e, f). Therefore, the larger contribution to the total error at EDW is from the bias or systematic model error. One possible explanation for this systematic model deficiency in forecast temperatures at EDW may be that the forecast point data extracted from the model are almost 250 m lower than the actual station elevation.

Figure 4.1. Bias, RMS error, and standard deviation of 2-m temperature (˚C) for XMR (solid lines), TBW (dotted lines), and EDW (dashed lines). Panels a (b), c (d), and e (f) show warm (cool) season error statistics plotted as a function of verification time.

4.1.2 2-m Dew Point Temperature

Biases in 2-m dew point temperatures at XMR and TBW during the warm season range generally within ±2 ˚C (Fig. 4.2a). At EDW, however, warm season dew point biases are mostly positive, with some values in excess of 4 ˚C. When viewed in conjunction with the 2-m temperature bias (Fig. 4.1a), the net effect is that warm season forecasts at EDW tend to be cool and moist, particularly during the first half of the forecast period. Another interesting point is that warm season standard deviations at EDW are greater than those at XMR and TBW with values ranging from about 2.5 to 4 ˚C (Fig. 4.2e). Since warm season dew point temperature biases and standard deviations are each relatively large at EDW, both systematic and non-systematic model errors make substantial contributions to the total RMS error for this location (Fig. 4.2c).

During the cool season, 2-m dew point temperature biases at all three stations are generally larger than warm season values (Fig. 4.2b). In particular, dew point temperature biases at TBW range from about –2 to 4 ˚C while at XMR, a moist bias of 3 to 4 ˚C is evident throughout much of the forecast cycle. Moreover, the gradual increase in bias and RMS error at XMR (Figs. 4.2b, d) indicates a decrease in forecast accuracy with time for this location. The difficulties in forecasting cool season 2-m dew point temperatures at XMR could be caused by excessive onshore surface winds (see section 4.1.4 below) leading to an overestimation of evaporation within the model's parameterized oceanic boundary layer. In fact, the vertical moisture flux from the model's oceanic sublayer is influenced by the Reynolds number which is a function of horizontal wind speed (Janjic 1994). One way to determine if dew point temperature errors are larger for onshore versus offshore flow would be to stratify the statistics by surface wind direction. In accordance with the original evaluation protocol, statistics were stratified by the 950- to 600-mb layer-average wind direction but did not reveal any substantial regime dependencies at either station. However, it is still possible that 2-m dew point temperature forecast errors are closely related to changes in surface wind direction/speed, especially at a coastal location such as XMR.

4.1.3 Mean Sea-Level Pressure

Biases in mean sea-level pressure (MSLP) at XMR and TBW are within ±1.5 mb throughout both seasonal evaluation periods (Figs. 4.3a, b). At EDW however, biases range from about –2 to 3.5 mb. In fact, cool season RMS errors at EDW increase with time from about 2 to 3.5 mb which indicates a gradual loss in forecast accuracy at that location (Fig. 4.3d). The 250 m elevation difference between forecasts and observations could again be one explanation for the MSLP errors encountered at EDW.

4.1.4 10-m Wind Speed

Warm season biases in the 10-m wind speed range from 0 to –5 m s^{-1} at EDW and from –1 to 2 m s^{-1} at XMR and TBW (Fig. 4.4a). In comparison, cool season biases range from 0 to –2 m s^{-1} at EDW and 0 to 3.5 m s^{-1} at XMR and TBW (Fig. 4.4b). Therefore, 10-m wind speed forecasts at XMR and TBW are generally too fast while those at EDW tend to be slow. Moreover, cool season wind speed biases at XMR are about 1 m s^{-1} faster than those during the warm season. In fact, increases in the bias and standard deviation during the cool season at XMR both combine to produce RMS errors which are about 1.5 m s^{-1} larger than observed during the warm season (Figs. 4.4c, d). Also of interest is the fact that warm season forecast errors at EDW follow a diurnal cycle with the largest values occurring between about 1500 and 0300 UTC (Figs. 4.4a, c, e).

Figure 4.2. Bias, RMS error, and standard deviation of 2-m dew point temperature (˚C) for XMR (solid lines), TBW (dotted lines), and EDW (dashed lines). Panels a (b), c (d), and e (f) show warm (cool) season error statistics plotted as a function of verification time.

Figure 4.3. Bias, RMS error, and standard deviation of mean sea-level pressure (mb) for XMR (solid lines), TBW (dotted lines), and EDW (dashed lines). Panels a (b), c (d), and e (f) show warm (cool) season error statistics plotted as a function of verification time.

Figure 4.4. Bias, RMS error, and standard deviation of 10-m wind speed (m s^{-1}) for XMR (solid lines), TBW (dotted lines), and EDW (dashed lines). Panels a (b), c (d), and e (f) show warm (cool) season error statistics plotted as a function of verification time.

One possible explanation for the increase in cool season wind speed biases at XMR may be a combination of model resolution and the fact that XMR is within about 3.5 km of the coast line. As winds move from sea to land an internal boundary layer develops quickly with distance from the shore (Powell et al. 1996). Enhanced surface friction over land slows observed winds within this boundary layer. Although these processes are parameterized in the meso-eta model's planetary boundary layer scheme (Janjic 1994), its 29-km grid point resolution is likely not sufficient to resolve the rapid decrease of wind speed due to friction within the short distance it is actually observed. The impact of this resolution shortcoming should be greater during the cool season with the occurrence of strong onshore gradient winds. As with the 2-m dew point temperature bias (section 4.1.2), these errors could be further investigated by performing wind regime stratifications based on the 10-m wind direction instead of the 950- to 600-mb layer-averaged wind direction specified for this study.

4.1.5 10-m Wind Direction

Biases in the 10-m wind direction during both warm and cool seasons exhibit a great deal of hour-to-hour fluctuation but are all within ±30˚ (Figs. 4.5a, b). Negative (positive) biases indicate that forecast wind directions are on average more counter-clockwise (clockwise) from the observed wind direction. Standard deviations range from about 30 to 90˚, indicating that much of the error is due to random, non-systematic type variabilities in wind direction (Figs. 4.5e, f). Since the model cannot temporally or spatially resolve many local effects which influence wind direction, especially when wind speeds are light, the magnitude of variability in wind direction errors is not surprising.

4.1.6 10-m Wind Speed Persistence

Because of their importance to operational evaluation of LCC and FR, meso-eta forecasts of 10-m wind speed are benchmarked against 1, 2, 3, and 6-h wind speed persistence forecasts. For example, 3-h persistence uses the current wind speed observation as a forecast for wind speeds at the same location three hours into the future. Persistence errors are calculated by subtracting the latest wind speed observation from the past observation, or persistence forecast. At XMR, mean errors in wind speed persistence forecasts during both seasons exhibit a diurnal cycle which increases in magnitude with lead time (Figs. 4.6a, b). Specifically, biases in the 1-h persistence forecasts are about 1.5 m s^{-1} smaller than those of the 6-h forecasts. It is not surprising that persistence forecasts tend to be slow (fast) around 1800 (0300) UTC since wind speeds generally increase (decrease) during daytime (nighttime) hours. RMS errors in persistence forecasts at XMR are mostly smaller than those of the meso-eta forecasts, especially during the cool season (Figs. 4.6c, d). These results suggest that, on average, persistence provides greater utility than the meso-eta model for 10-m wind speed forecasts at XMR.

At TBW, a diurnal cycle appears in the wind speed persistence biases (Figs. 4.7a, b) which is nearly identical in timing and magnitude to that observed at XMR (Figs. 4.6a, b). Again, note that biases in the 1-h persistence forecasts are about 1.5 m s^{-1} smaller than those of the 6-h forecasts. On the other hand, model forecast biases and RMS errors at TBW (Figs. 4.7a-d) are slightly smaller than those at XMR (Figs. 4.6a-d), particularly during the cool season. As a result of this subtle decrease in model error at TBW, meso-eta forecasts of 10-m wind speed are occasionally more accurate than 3-h and 6-h persistence forecasts.

Biases in wind speed persistence forecasts at EDW range from ±1 m s^{-1} at 1 h to ±4 m s^{-1} at 6 h (Figs. 4.8a, b). However, biases and RMS errors for meso-eta wind speed forecasts are mostly larger than those made by persistence (Figs. 4.8a-d). Therefore, persistence usually provides greater accuracy than the meso-eta model in 10-m wind speed forecasts at EDW.

Figure 4.5. Bias, RMS error, and standard deviation of 10-m wind direction (˚) for XMR (solid lines), TBW (dotted lines), and EDW (dashed lines). Panels a (b), c (d), and e (f) show warm (cool) season error statistics plotted as a function of verification time.

Figure 4.6. Bias, RMS error, and standard deviation of 10-m wind speed persistence (m s^{-1}) and forecast 10-m wind speed (m s^{-1}) for XMR. Wind speed persistence at 1, 2, 3, and 6-h are shown with thin solid, dotted, short-dashed, and long dashed lines, respectively. The thick solid line in each panel depicts the corresponding error statistic for 10-m wind speed as shown in Fig. 4.4. Panels a (b), c (d), and e (f) show warm (cool) season error statistics plotted as a function of verification time.

Figure 4.7. Bias, RMS error, and standard deviation of 10-m wind speed persistence (m s^{-1}) and forecast 10-m wind speed (m s^{-1}) for TBW. Wind speed persistence at 1, 2, 3, and 6-h are shown with thin solid, dotted, short-dashed, and long dashed lines, respectively. The thick solid line in each panel depicts the corresponding error statistic for 10-m wind speed as shown in Fig. 4.4. Panels a (b), c (d), and e (f) show warm (cool) season error statistics plotted as a function of verification time.

Figure 4.8. Bias, RMS error, and standard deviation of 10-m wind speed persistence (m s^{-1}) and forecast 10-m wind speed (m s^{-1}) for EDW. Wind speed persistence at 1, 2, 3, and 6-h are shown with thin solid, dotted, short-dashed, and long dashed lines, respectively. The thick solid line in each panel depicts the corresponding error statistic for 10-m wind speed as shown in Fig. 4.4. Panels a (b), c (d), and e (f) show warm (cool) season error statistics plotted as a function of verification time.

4.1.7 10-m Wind Direction Persistence

Biases in both model and persistence forecasts of wind direction at XMR range from about –30 to 15˚ but vary widely by hour (Figs. 4.9a, b). In comparison, standard deviations of wind direction errors range from about 30 to 90˚ (Figs. 4.9e, f). These results suggest that substantial variability is present in both model and persistence forecasts of wind direction. RMS errors in model forecast wind directions are generally comparable in magnitude to those of the 3-h and 6-h persistence forecasts (Figs. 4.9c, d). Therefore, the utility provided by meso-eta forecasts of 10-m wind direction may be comparable to the use of persistence forecasts with lead times greater than 3 hours. The same discussion applies to model and persistence forecasts of 10-m wind direction errors at TBW (Fig. 4.10).

Biases in both model and persistence forecasts of wind direction at EDW are within about ±30˚ but vary widely by hour (Figs. 4.11a, b). A diurnal cycle is evident as maximum (minimum) errors occur around 0900 (1800) UTC. During the warm season, this diurnal cycle is also apparent in both the RMS errors and standard deviations as values range widely from about 30 to 90˚ (Figs. 4.11c, e). RMS errors and standard deviations are slightly larger during the cool season, with values ranging from about 60 to 90˚ (Figs. 4.11d, f). Since model forecast errors of wind direction at EDW during both seasons lie within the range of errors produced by persistence forecasts, Fig. 4.11 collectively demonstrates that model forecasts are comparable in accuracy with 2 to 3-h persistence forecasts.

4.1.8 Forecast Consistency

As described in section 3.2 (Eq. 5), forecast consistency describes the average difference between subsequent forecasts verifying at the same time but initialized 12-h apart. Again, smaller (larger) values of consistency indicate that on average model runs agree more (less) closely with one another. Although consistency calculations compare two subsequent forecasts valid at the same time, results are presented as a function of forecast duration from 12- to 33-h. This is done because direct forecast comparisons are independent of real time and because this method of presentation emphasizes the 12-h lag between subsequent forecasts. Therefore, graphs shown on the left (right) hand side of Figs. 4.12 and 4.13 present results determined by subtracting newer 1500 (0300) UTC forecasts from older 0300 (1500) UTC forecasts from 12-h through 33-h.

For most parameters, consistency between subsequent model runs are smaller than the corresponding biases, especially toward the end of the forecast period (Figs. 4.12 and 4.13). For example, 10-m wind speed consistency is smaller than the 10-m wind speed bias shown in Fig. 4.4. Also, at forecast hour twelve (12), 2-m dew point temperature consistency during the cool season at XMR is near 2 ˚C (Fig. 4.13d) while the bias in 2-m dew point temperature at XMR reaches nearly 4 ˚C (Fig. 4.2b). These results suggest that model forecasts tend to agree more closely with one another than with observations. Several parameters such as 2-m temperature, 2-m dew point temperature, and 10-m wind speed exhibit larger values of consistency at the beginning of the verification period than towards the end of the period. This result may be explained by reiterating that consistency at the start of the verification period measures differences between older 12-h forecasts and newer 0-h forecasts updated with observations. At later forecast hours, the observation-based initial conditions have less impact on the model's depiction of the atmosphere. Therefore, certain parameters tend to become more consistent with time as the forecasts respond less to forcing by the initial

conditions.

Figure 4.9. Bias, RMS error, and standard deviation of 10-m wind direction persistence (˚) and forecast 10-m wind direction (˚) for XMR. Wind direction persistence at 1, 2, 3, and 6-h are shown with thin solid, dotted, short-dashed, and long dashed lines, respectively. The thick solid line in each panel depicts the corresponding error statistic for 10-m wind direction as shown in Fig. 4.5. Panels a (b), c (d), and e (f) show warm (cool) season error statistics plotted as a function of verification time.

Figure 4.10. Bias, RMS error, and standard deviation of 10-m wind direction persistence (˚) and forecast 10-m wind direction (˚) for TBW. Wind direction persistence at 1, 2, 3, and 6-h are shown with thin solid, dotted, short-dashed, and long dashed lines, respectively. The thick solid line in each panel depicts the corresponding error statistic for 10-m wind direction as shown in Fig. 4.5. Panels a (b), c (d), and e (f) show warm (cool) season error statistics plotted as a function of verification time.

Figure 4.11. Bias, RMS error, and standard deviation of 10-m wind direction persistence (˚) and forecast 10-m wind direction (˚) for EDW. Wind direction persistence at 1, 2, 3, and 6-h are shown with thin solid, dotted, short-dashed, and long dashed lines, respectively. The thick solid line in each panel depicts the corresponding error statistic for 10-m wind direction as shown in Fig. 4.5. Panels a (b), c (d), and e (f) show warm (cool) season error statistics plotted as a function of verification time.

Figure 4.12. Warm season forecast consistency of temperature (˚C), dew point temperature (˚C), mean sea-level pressure (mb), wind speed (m s^{-1}), and wind direction (˚) at XMR (solid lines), TBW (dotted lines), and EDW (dashed lines). Panels a (b), c (d) , e (f) , g (h) , and i (j) show consistency calculated by subtracting newer 1500 (0300) UTC forecasts from older 0300 (1500) UTC forecasts plotted as a function of forecast duration. Consistency plots begin at forecast hour twelve (12) because subsequent forecasts initialized 12-h apart first overlap at that time.

Figure 4.13. Cool season forecast consistency of temperature (˚C), dew point temperature (˚C), mean sea-level pressure (mb), wind speed (m s^{-1}), and wind direction (˚) at XMR (solid lines), TBW (dotted lines), and EDW (dashed lines). Panels a (b), c (d) , e (f) , g (h) , and i (j) show consistency calculated by subtracting newer 1500 (0300) UTC forecasts from older 0300 (1500) UTC forecasts plotted as a function of forecast duration. Consistency plots begin at forecast hour twelve (12) because subsequent forecasts initialized 12-h apart first overlap at that time.

4.2 Upper Air Forecasts

Examination of all statistics for the upper air parameters outlined in section 3.2 does not reveal any substantial differences between the 0300 and 1500 UTC forecast cycles. Moreover, the statistics do not reveal any obvious differences when the results are stratified by the 950- to 600-mb layer-averaged wind direction. For example, biases generally occur with comparable magnitudes at about the same height regardless of forecast cycle or wind regime classification. In light of these findings, the bias, RMS error, and standard deviation at XMR, TBW, and EDW are presented by season as a function of pressure and verification period. In addition to the graphical results, tables are presented in the Appendix which list biases and RMS errors in u and v wind components, wind speed, and wind direction as a function of height and verification period for XMR and EDW. These statistics are listed in tabular format for general interest and applications to Shuttle landing flight rules.

Since each verification period defined in section 3.2 corresponds to forecasts of greater duration, direct comparison of RMS errors from each period enables the identification of possible error growth with time. However, examination of results presented below indicates that steady or substantial increases in error with time only occur in a few instances.

4.2.1 Geopotential Height

To diagnose errors in geopotential height forecasts, GEMPAK was used to extract or calculate all upper air parameters from both forecast and observed sounding data at their reported levels. These parameters are then input into a program which log-linearly interpolates the data to specified pressure and height levels before computing statistics as described in section 3.2. After the statistics were computed, vertical profiles of geopotential height error were noisy because observed heights at mandatory levels are reported and stored directly in GEMPAK sounding files whereas heights at other significant levels are computed by GEMPAK using reported values of temperature and dew point temperature. This discrepancy could be corrected by first interpolating all forecast and observed temperatures and dew point temperatures to the desired verification levels. Then moist hydrostatic heights can be derived using the same method at all levels prior to computing the bias, RMS error, and standard deviation. Because the problem was discovered late in the evaluation period, there was not sufficient time to update the software and recompute the statistics. Therefore, geopotential height errors are not presented in this report. Since derived heights are closely tied to virtual temperature, larger height errors should be expected at those levels where large temperature and moisture errors are reported.

4.2.2 Temperature

Warm season temperature forecasts at EDW are nearly unbiased except above the tropopause and at levels below 850 mb (Fig. 4.14c). At XMR and TBW, biases below 700 mb are about 1 ˚C colder than observed whereas above 600 mb they are nearly 2 ˚C warmer than observed (Figs. 4.14a, b). The net effect for warm season forecasts at these Florida stations is a tendency towards a thermally stable model atmosphere. Below the tropopause, standard deviations (Figs 4.14g, h, i) indicate that random, non-systematic errors in the forecasts are about 1 ˚C. In comparison, typical RMS uncertainty in rawinsonde temperature observations is about 0.6 ˚C (Hoehne 1980; Ahnert 1991) which suggests that more than half of the non-systematic error may be due to measurement uncertainty.

During the cool season, temperature forecasts at EDW exhibit a cool bias below 700 mb of 1 to 2 ˚C (Fig. 4.15c). At XMR and TBW, temperature errors above 600 mb and below 850 mb average about 1 ˚C warmer than observations (Fig. 4.15a, b). In between, there is a sharp cold bias of nearly –2 ˚C around the 750 mb level. Examination of forecast and observed soundings at XMR throughout

the cool season (not shown) reveals that this cold bias appears primarily because model forecasts of the lower tropospheric inversion are frequently stronger and higher than actually observed.

Figure 4.14. Warm season bias, RMS error, and standard deviation of temperature (˚C) plotted as a function of pressure level for XMR (panels a, d, g), TBW (panels b, e, h), and EDW (panels c, f, i). The solid, dotted, and dashed lines show the corresponding error statistics for verification periods 1, 2, and 3, respectively. The verification periods are defined in Fig. 3.1.

Figure 4.15. Cool season bias, RMS error, and standard deviation of temperature (˚C) plotted as a function of pressure level for XMR (panels a, d, g), TBW (panels b, e, h), and EDW (panels c, f, i). The solid, dotted, and dashed lines show the corresponding error statistics for verification periods 1, 2, and 3, respectively. The verification periods are defined in Fig. 3.1.

4.2.3 Mixing Ratio

Warm season mixing ratio biases at XMR and TBW (Figs. 4.16a, b) indicate that meso-eta forecasts are generally too dry in the lower troposphere, most notably at XMR. Conversely, biases above 500 mb suggest that forecasts at these locations tend to retain larger amounts of moisture than observed. In combination with the cool lower tropospheric temperature biases discussed in the previous section, these results suggest that warm season model forecasts at XMR and TBW are typically more stable than observed. Section 4.3 will demonstrate that stability index errors also indicate a stable bias. At EDW, middle tropospheric mixing ratio biases are near zero during the warm season (Fig. 4.16c). However, upper and lower tropospheric forecasts at EDW tend to retain larger amounts of moisture than observed. During the cool season, mixing ratio biases at all three stations are slightly wet or near zero at most levels (Figs. 4.17a, b, c) except for the dry layer which appears between 950 and 800 mb at XMR and TBW.

RMS errors for both warm and cool seasons (Figs. 4.16-4.17d, e, f) drop from around 2 g kg^{-1} at low-levels (1.5 g kg^{-1} at EDW) to near zero at 200 mb, where there is very little water vapor present in the atmosphere. At XMR and TBW in particular, it is interesting to note that warm season RMS errors in the lower troposphere increase slightly with verification period, thereby indicating a growth in forecast error with time (Figs. 4.17d, e). Results shown in Figs. 4.16-4.17d-f are consistent with those of Rogers et. al (1996), who show 24-h RMS errors in specific humidity from 48-km eta model forecasts across the United States during September 1994 ranging from nearly 2 g kg^{-1} at 1000 mb to less than 0.1 g kg^{-1} at 250 mb (see their Fig. 7). Note that these calculations for mixing ratio errors are not normalized by magnitude and are therefore not representative of percent errors as the mixing ratio tends toward zero in the upper troposphere.

4.2.4 Wind Speed

Warm season wind speed biases below the tropopause at XMR and TBW are less than ±1 m s^{-1} (Figs. 4.18a, b). Forecast wind speeds at EDW are about 2 m s^{-1} slower than observed, especially in the lower troposphere (Fig. 4.18c). Below the tropopause, RMS errors at XMR and TBW slightly exceed 2 m s^{-1} while at EDW they reach nearly 4.5 m s^{-1} (Figs. 4.18d, e, f). Moreover, RMS errors in wind speed forecasts at EDW appear to increase with verification period by about 1 m s^{-1} which indicates error growth with time. Since biases are small at all three stations, these results suggest that the model suffers little systematic error in wind speeds. In fact, relatively large standard deviations of 2 to 5 m s^{-1} (Figs. 4.18g, h, i) reveal that random variations in forecast and/or observed wind speeds account for a large portion of the total wind speed error. For comparison, uncertainties in rawinsonde wind speed measurements are about 3.1 m s^{-1} (Hoehne 1980), which suggests that a large component of the total wind speed error may result from observational uncertainties in wind speed.

During the cool season, wind speed biases at XMR and TBW are less than ±1.5 m s^{-1} (Figs. 4.19a, b). At EDW, wind speed biases exhibit strong variations with height but remain within ±2 m s^{-1} (Fig. 4.19c). RMS errors at XMR and TBW range from 2 m s^{-1} in the lower troposphere to just over 4 m s^{-1} in the upper troposphere while at EDW, errors reach nearly 6 m s^{-1} (Figs. 4.19d, e, f). As in the warm season, the increase in middle tropospheric RMS errors with verification period at EDW suggests that forecast errors grow with time for this location. The relatively large standard deviations of 2 to 6 m s^{-1} (Figs. 4.19g, h, i) also indicate that as in the warm season, non-systematic variations in forecast and/or observed wind speeds account for a large portion of the total wind speed error.

Figure 4.16. Warm season bias, RMS error, and standard deviation of mixing ratio (gm kg^{-1}) plotted as a function of pressure level for XMR (panels a, d, g), TBW (panels b, e, h), and EDW (panels c, f, i). The solid, dotted, and dashed lines show the corresponding error statistics for verification periods 1, 2, and 3, respectively. The verification periods are defined in Fig. 3.1.

Figure 4.17. Cool season bias, RMS error, and standard deviation of mixing ratio (gm kg^{-1}) plotted as a function of pressure level for XMR (panels a, d, g), TBW (panels b, e, h), and EDW (panels c, f, i). The solid, dotted, and dashed lines show the corresponding error statistics for verification periods 1, 2, and 3, respectively. The verification periods are defined in Fig. 3.1.

Figure 4.18. Warm season bias, RMS error, and standard deviation of wind speed (m s^{-1}) plotted as a function of pressure level for XMR (panels a, d, g), TBW (panels b, e, h), and EDW (panels c, f, i). The solid, dotted, and dashed lines show the corresponding error statistics for verification periods 1, 2, and 3, respectively. The verification periods are defined in Fig. 3.1.

Figure 4.19. Cool season bias, RMS error, and standard deviation of wind speed (m s^{-1}) plotted as a function of pressure level for XMR (panels a, d, g), TBW (panels b, e, h), and EDW (panels c, f, i). The solid, dotted, and dashed lines show the corresponding error statistics for verification periods 1, 2, and 3, respectively. The verification periods are defined in Fig. 3.1.

4.2.5 Wind Direction

Warm season wind direction forecasts at XMR and TBW are nearly unbiased, as mean errors lie within ±10˚ (Figs. 4.20a, b). Biases at EDW are within ±20˚ and demonstrate greater variability with height, especially within the lower troposphere (Fig. 4.20c). Moreover, warm season wind direction forecasts at EDW are typically negative, or counter-clockwise relative to observed values except for the 750 to 850 mb layer where biases for verification periods 2 and 3 are positive. Although forecast wind direction biases are reasonably small, RMS errors and standard deviations approach 60˚ and are nearly twice as large at XMR and TBW as they are at EDW (Figs. 4.20d-i). Hoehne (1980) reports that observational uncertainty in wind direction decreases with increasing wind speeds from 14˚ at 10 kt to 2˚ at 120 kt. In addition to the fact that observational uncertainty for wind direction is a function of wind speed, the accuracy of forecast wind directions may also be influenced by wind speed. At most levels, average warm season observed wind speeds (not shown) at EDW are about 5 to 15 kt faster than those at XMR and TBW with larger differences occurring in the upper troposphere. Average warm season forecast wind speeds exhibit the same characteristics. Since mean forecast and observed wind speeds are faster at EDW, it is not surprising that standard deviations in wind direction are smaller at EDW than those at XMR and TBW. That is, the difference in wind direction standard deviations between EDW and XMR and TBW could be accounted for, in part, by difficulties in both observing and forecasting wind directions accurately at low wind speeds.

Cool season errors in wind direction forecasts are similar to those of the warm season with a few exceptions (Fig. 4.21). First, while there is no longer a lower tropospheric positive bias in wind direction forecasts at EDW, a positive bias does appear for lower tropospheric wind directions at TBW (Figs. 4.21b, c). Second, RMS errors and standard deviations at XMR and TBW decrease relative to warm season values above 700 mb (Figs. 4.21d, e, g, h). During the cool season, both forecast and observed average wind speeds (not shown) increase relative to warm season speeds by about 15 to 25 kt at XMR and TBW. Therefore, the upper tropospheric decrease in RMS errors and standard deviations in wind direction at XMR and TBW could again be explained by the idea that both forecast and observed wind directions are more accurate at higher wind speeds.

4.2.6 Consistency

Model forecast consistency for upper air data is calculated as a function of pressure and time (Eq. 5). As with the surface consistency calculations discussed in section 4.1.8, upper air calculations begin 12-h into the older forecast and proceed through the end of 33-h forecast period. However, since upper air calculations have the additional pressure-level dimension, only consistency values at 12, 21, and 30 h are presented for brevity. These times are selected because they represent values at even intervals which correspond to the beginning, middle, and end of the period over which consistency is calculated. Moreover, these times match reasonably well with each of the three periods defined in section 3.2 for verification of upper air forecasts with observations. Because there are no substantial diurnal signatures in the upper air consistency values, the results plotted in Figs. 4.22 and 4.23 make use of all available forecasts from both the 0300 UTC and 1500 UTC forecast cycles.

Examination of Figs. 4.22 and 4.23 reveals that upper air consistency values are small compared to the corresponding forecast biases shown previously in Figs. 4.14-4.21. That is, the average difference between subsequent forecasts is small relative to the mean forecast error. Larger differences are commonly found at 12 h (solid line in Figs. 4.22 and 4.23), which measures the consistency between the current 0-h initialization/forecast and the 12-h forecast from the previous model run. The fact that larger differences are found for upper air consistency more often at 12 h

rather than at 21 h or 30 h is not surprising because newer forecasts are updated with observations at 12 h, as discussed for surface consistency calculations in section 4.1.8.

Figure 4.20. Warm season bias, RMS error, and standard deviation of wind direction (˚) plotted as a function of pressure level for XMR (panels a, d, g), TBW (panels b, e, h), and EDW (panels c, f, i). The solid, dotted, and dashed lines show the corresponding error statistics for verification periods 1, 2, and 3, respectively. The verification periods are defined in Fig. 3.1.

Figure 4.21. Cool season bias, RMS error, and standard deviation of wind direction (˚) plotted as a function of pressure level for XMR (panels a, d, g), TBW (panels b, e, h), and EDW (panels c, f, i). The solid, dotted, and dashed lines show the corresponding error statistics for verification periods 1, 2, and 3, respectively. The verification periods are defined in Fig. 3.1.

Figure 4.22. Warm season forecast consistency of temperature (˚C), mixing ratio (gm kg^{-1}), wind speed (m s^{-1}), and wind direction (˚) plotted as a function of pressure at XMR (panels a, d, g, j), TBW (panels b, e, h, k), and EDW (panels c, f, i, l). The solid, dotted, and dashed lines show forecast consistency at 12-h, 21-h, and 30-h, respectively. See text for details of verification times.

Figure 4.23. Cool season forecast consistency of temperature (˚C), mixing ratio (gm kg^{-1}), wind speed (m s^{-1}), and wind direction (˚) plotted as a function of pressure at XMR (panels a, d, g, j), TBW (panels b, e, h, k), and EDW (panels c, f, i, l). The solid, dotted, and dashed lines show forecast consistency at 12-h, 21-h, and 30-h, respectively. See text for details of verification times.

Many characteristic forecast biases identified in Figs. 4.14-4.21 appear, particularly with the 12-h consistency values, in the consistency profiles shown in Figs. 4.22 and 4.23. For example, the cool/dry nature of lower tropospheric warm season forecasts at XMR and TBW is discernible in the temperature and mixing ratio consistency profiles shown in Figs. 4.22a, b, d, and e. Similarly, the model's tendency to forecast cool season lower tropospheric temperature inversions which are higher and stronger than observed at XMR and TBW is evident between 600 and 800 mb (Figs. 4.23a, b). Wind speeds exhibit larger inconsistencies in the upper troposphere during both seasons, while wind direction changes are within ±10˚. Overall, subsequent forecasts of upper air parameters tend to be more consistent with each other than with observations. Moreover, the differences between subsequent forecasts are in agreement with the forecast biases identified in sections 4.2.2 through 4.2.5.

4.3 Convective Indices

The bias and RMS error for warm and cool season convective indices described in section 3.2 (Table 3.1) are presented in Table 4.1 for XMR and TBW as a function of verification period. Results for EDW are not shown because convection is usually not a concern at that location. The convective parameters shown in Table 4.1 are typically used to help forecast the probability of thunderstorm occurrence on a given day. Convective activity is almost certain to occur, for example, when the KINX approaches 40. When used alone, the errors in forecast convective parameters such as KINX on a particular day may actually be large enough to provide misleading information regarding the likelihood for thunderstorm development.

Statistical calculations were performed using all available data from both the 0300 UTC and 1500 UTC model runs and corresponding observations. Although calculations were originally stratified by forecast cycle and 950- to 600-mb layer-averaged wind regime, only the combined results are shown since no substantial differences were identified in the stratified statistics. Standard deviations are omitted because in most cases they are similar in magnitude to the RMS errors and because they can be calculated directly using Eq. 4.

Table 4.1. Bias and RMS error for warm and cool season convective parameters at XMR and TBW. See Fig. 3.1 and Table 3.1 for definitions of verification periods and convective parameter acronyms, respectively.

	Ver	PWAT		CAPE		CINS		LIFT		KINX		HLCY		MDPI	
	Per.	XMR	TBW	XMR	TBW	XMR	TBW	XMR	TBW	XMR	TBW	XMR	TBW	XMR	TBW
Warm	1	-1.6	-0.2	-712	-302	9	-12	1.8	1.0	-0.1	1.5	4	-1	.18	.20
Season	2	-2.2	-0.1	-758	-435	1	-23	2.1	1.3	2.2	1.1	6	5	.17	.14
Bias	3	-2.7	-0.5	-944	-444	-9	-23	2.9	1.8	-2.3	0.7	11	3	.22	.14
Cool	1	1.2	-0.3	2	16	2	4	-0.1	-0.1	4.0	2.2	16	13	.17	.18
Season	2	0.8	-0.5	20	29	6	9	-0.3	-0.3	2.7	1.4	6	9	.22	.18
Bias	3	0.5	-0.5	36	12	2	5	-0.5	-0.2	3.0	2.9	15	14	.23	.14
Warm	1	4.0	4.8	1261	871	68	53	2.8	2.4	5.8	7.0	33	36	.21	.24
Season	2	4.9	5.4	1235	870	46	63	3.1	2.6	6.7	7.1	36	34	.21	.16
RMS Error	3	5.6	4.9	1351	931	48	51	3.5	2.8	6.9	7.1	38	36	.25	.17
Cool	1	3.7	3.7	246	158	31	40	2.2	2.2	10.5	8.8	64	65	.21	.22
Season	2	3.9	3.9	224	141	28	48	2.5	2.4	11.1	9.4	61	69	.26	.21
RMS Error	3	4.9	4.8	250	123	24	46	2.7	2.6	12.0	11.4	72	73	.28	.18

During the warm season, negative biases in PWAT and CAPE and positive biases in LIFT suggest that forecast soundings are typically drier and more stable than observed (Table 4.1). In particular, CAPE forecasts at XMR are nearly 1000 J kg^{-1} smaller than observed values and RMS errors exceed 1200 J kg^{-1}. These errors are consistent with upper air warm season biases in mixing ratio and temperature at XMR which indicate that forecasts tend to be thermodynamically more stable than observed (Figs. 4.14 and 4.16). Later in section 5, it will be demonstrated that the meso-eta model typically generates warm season precipitation over Florida too early in the day. One possible explanation for this discrepancy between overly stable forecast soundings and excessive precipitation is that the model erodes the stable surface layer and breaks the capping inversion more quickly and vigorously than observed. Unfortunately, rawinsonde data are not consistently available at sufficient temporal resolution throughout the daytime hours to validate this hypothesis.

Cool season biases and RMS errors in PWAT and CAPE are mostly smaller than the corresponding warm season errors. Although the meso-eta model may actually be forecasting these indices more accurately during the cool season, another possible reason for the decrease in error may result from the fact that forecast and observed values of PWAT and CAPE are generally smaller during the cool season. Positive biases in CAPE and KINX and negative biases in LIFT suggest that cool season forecasts are more unstable than observed (Table 4.1). These results are consistent with the warm and moist unstable cool season temperature and mixing ratio biases shown at low-levels in Figs. 4.15 and 4.17. Cool season RMS errors for KINX increase relative to warm season errors. KINX measures instability based on the 850- to 500-mb lapse rate, the 850-mb dew point temperature, and the 700-mb dew point depression. Examination of biases for each of these parameters reveals that the 700-mb cold bias in temperature (Figs. 4.15a, b) makes the strongest contribution to the cool season KINX errors.

Positive biases in MDPI during both warm and cool seasons indicate that on average the model tends to overforecast the potential for microburst development at XMR and TBW based on environmental lapse rates of equivalent potential temperature (Wheeler and Roeder 1996). Biases in HLCY are also slightly positive during both seasons, except for verification period 1 at TBW. While HLCY biases are small, RMS errors during the cool season are nearly double those for the warm season. Since HLCY biases are small and contribute little to the total RMS error, much of the total RMS error develops in response to non-systematic variabilities in forecasts and/or observations of HLCY (Eq. 4, section 3.2). Since HLCY is a measure of the vertically-integrated wind shear over the lowest 3 km of the atmosphere, this variability is consistent with the large standard deviations previously noted in section 4.2.5 with regard to wind direction errors (Figs. 4.20, 4.21). Increases in RMS errors for HLCY from the warm to cool season may occur because mean cool season forecast and observed wind speeds and corresponding wind shear are larger than those during the warm season.

4.4 850 to 500-mb Layer-Averages

The bias and RMS error for warm and cool season 850 to 500-mb layer-averaged winds and relative humidity are presented for XMR, TBW, and EDW in Table 4.2 as a function of verification period. In addition to the layer-averaged wind speed and direction errors, statistics are included for the u and v wind components for application to LCC and Shuttle FR. As with convective parameters, calculations were performed using all available data from both the 0300 and 1500 UTC model runs and corresponding observations. Although calculations were originally stratified by forecast cycle and 950- to 600-mb layer-averaged wind regime, only the combined results are shown since no substantial differences were identified in the stratified statistics. Standard deviations are omitted because in most cases they are similar in magnitude to the RMS errors and because they can be directly calculated using Eq. 4.

Table 4.2. Warm and cool season bias and RMS error for 850- to 500-mb layer-averaged *u*-, and *v*-wind components, wind speed and wind direction. See Fig. 3.1 for definitions of verification periods.

	Ver Per.	Rel. Humidity (%)			U-wind (m s^{-1})			V-wind (m s^{-1})			Wind Speed (m s^{-1})			Wind Direction (°)		
		XMR	TBW	EDW	XMR	TBW	EDW	XMR	TBW	EDW	XMR	TBW	EDW	XMR	TBW	EDW
Warm	1	-1	3	2	-1.3	-0.8	-0.8	-0.3	-0.1	0.7	0.0	0.3	-0.7	-5	-2	-9
Season	2	-3	2	0	-0.1	-0.7	-0.3	0.0	-0.4	-0.3	0.0	0.2	-1.0	-4	-7	-3
Bias	3	-2	4	0	-0.3	-0.9	-0.9	0.1	-0.1	0.2	0.2	0.4	-1.3	-5	-8	-9
Cool	1	2	1	2	-1.0	-1.0	-0.9	0.2	0.0	0.7	-0.7	-0.2	-0.3	-3	-2	-4
Season	2	2	2	0	-0.6	-0.6	-1.6	0.1	-0.1	0.5	-0.4	-0.2	-0.6	-2	-2	-8
Bias	3	1	1	1	-0.6	-0.7	-2.4	0.0	-0.2	0.8	-0.2	0.1	-1.1	-2	-4	-10
Warm	1	10	11	6	2.1	1.7	2.0	1.6	1.3	1.7	1.9	1.8	1.7	35	31	17
Season	2	12	13	6	1.7	1.7	2.4	1.8	1.6	2.2	1.8	1.7	2.1	34	36	33
RMS Error	3	13	13	6	1.9	2.3	2.8	2.1	2.0	2.2	2.1	2.0	2.8	39	47	28
Cool	1	11	10	8	1.5	1.6	1.9	1.4	1.3	2.1	1.5	1.7	1.7	20	22	12
Season	2	12	10	9	1.6	1.9	2.5	1.6	1.5	2.5	1.7	1.7	2.3	21	22	30
RMS Error	3	14	12	9	1.9	2.1	3.2	1.9	2.0	2.6	2.1	2.3	2.7	26	31	40

In general, the results shown in Table 4.2 are consistent with the discussion and figures presented in section 4.2. Biases in relative humidity (RH) at all three stations are near zero during both seasons with corresponding RMS errors of 5-10% at EDW and 10-15% at XMR and TBW. Observational uncertainty in rawinsonde observations of RH are about 2.5% (Ahnert 1991) which may provide a strong contribution to the total error in RH forecasts. Because RH varies non-linearly with the saturation mixing ratio, direct comparisons cannot be made with the mixing ratio errors shown in Figs. 4.16 and 4.17. However, it is interesting to note that the sign of RH biases shown in Table 4.2 generally correspond well with the sign of mixing ratio biases in the levels between 850 to 500 mb (Figs. 4.16 and 4.17).

RMS errors for *u* and *v* wind component forecasts at all three stations range from about 1.5 to 3.2 m s^{-1} during both warm and cool seasons. Negative biases in the *u*-component winds indicate that forecasts are typically slower than observations while biases in the *v*-component winds are closer to zero. Since *u* and *v* wind components make up the total wind speed, it is not surprising that RMS errors in wind speed also range from about 1.5 to 2.8 m s^{-1}. These results for wind speed errors (Table 4.2) are consistent with the statistics at individual levels from 850 to 500 mb (Figs. 4.18 and 4.19). Biases in wind direction range from -2 to -10˚, thereby indicating that forecast wind directions in the 850 to 500-mb layer tend to be counterclockwise relative to observed directions. RMS errors in wind direction are largest during the warm season with values ranging from 17 to 47˚. The smaller cool season RMS errors range from 12 to 40˚. The small biases and relatively larger RMS errors in 850- to 500-mb layer-averaged wind direction forecasts are consistent with results discussed in section 4.2.5 and shown in Figs. 4.20 and 4.21. Particularly, the large RMS errors are indicative of substantial variability in the forecast and/or observed wind directions. Moreover, the decrease in cool season RMS errors relative to warm season values are consistent with the fact that measurement uncertainty decreases with increasing wind speeds.

5.0 Results of Subjective Evaluation

The results presented in this section focus on the subjective verification of sea breezes, thunderstorms, tropical waves, cold fronts, winds, and clouds. The subjective component of the overall meso-eta model evaluation is designed to assess the added value of the meso-eta model in forecasting selected aspects of these phenomenon. The evaluation strategy for sea breezes and thunderstorms consists of limited case studies of selected events and a seasonal verification on all days during the warm season when both observational and forecast data are available. A similar procedure is followed for the verification of cold fronts using data collected during the cool season. The verification of tropical waves during the warm season is limited by the availability of observed cases which were present within the subset domain of gridded forecast data. Finally, case studies of interesting wind and cloud forecasts are not performed for reasons discussed in sections 5.5 and 5.6, respectively.

5.1 Sea-Breeze Verification

The sea/land breeze is a well-documented mesoscale circulation that affects many coastal areas of the world including the peninsula of Florida (Pielke and Segal 1986). Numerous observational (e.g. Blanchard and Lopez 1985) and numerical (e.g. Pielke 1974; Boybeyi and Raman 1992) studies have demonstrated how the timing and location of convection across Florida is often modulated by local interactions between the sea-breeze circulation and prevailing synoptic-scale wind. With its 29-km grid point spacing, the horizontal resolution of the meso-eta model is too coarse to resolve the detailed, mesoscale structure of both the east and west coast sea breezes that are common along the Florida coastlines during the warm season. Nevertheless, the model can forecast certain characteristics of the observed sea breeze including a thermally direct circulation that results from differential low-level heating across the land/sea interface. The verification consists of both a case study and statistics that show how reliably the model can forecast the occurrence of the sea breeze over Florida during the warm season from May through August 1996.

5.1.1 Case Example

The example presented here is an analysis of forecast and observed sea-breeze development over the Florida peninsula on 7 June 1996. This case is chosen because it illustrates the typical 29-km eta model signature of the sea breeze that is often forecast during the warm season. Another reason for selecting 7 June is the availability of both model and observational data needed for the analysis. The following sections present observations of the sea breeze followed by an examination of the meso-eta forecast to distinguish clearly the model capabilities and limitations in depicting the structure and evolution of the sea-breeze circulation.

5.1.1.1 Observations

A limited synoptic overview of the large-scale conditions at 1200 UTC 7 June 1996 is shown in Fig. 5.1. This analysis is obtained from the 0-h forecast of the 48-km eta model run initialized at 1200 UTC 7 June 1996. At that time, the Florida peninsula is under the influence of a ridge axis oriented west-to-east across the central portion of the state (Fig. 5.1) and a closed high in the Gulf of Mexico, as shown by the 850 mb geopotential heights in Fig. 5.1. The 950- to 650-mb layer-averaged wind vectors reveal that lower tropospheric winds are light (≤ 5 kt) and variable over Florida in association with weak geopotential height gradients. Surface winds (not shown) along the east and west coasts of Florida are also light and variable with offshore components along sections of both coasts.

A peninsula-scale perspective of the sea breeze along Florida's east and west coasts is shown in the 4-km GOES visible imagery (Fig. 5.2). The development and movement of the sea breeze is inferred from the location of narrow bands of shallow cumulus clouds. It is important to point out that sea-breeze circulations are likely present before their signatures appear as bands of visible clouds (Weckwerth et al. 1997). However, this limitation is not critical for the case presented here since the visible imagery is used to illustrate the qualitative features of the sea breeze rather than to estimate its onset time and/or propagation speed.

Figure 5.1. Synoptic overview from 0-h forecast of the 48-km eta model run initialized at 1200 UTC 7 June 1996. The 850 mb geopotential heights (m) contoured every 5 m are shown by thick solid lines. Vectors represent the 950- to 650-mb layer-averaged winds. The vector length is proportional to wind speed with a representative 5-kt vector shown in the upper right corner of the figure. The larger and smaller subset boxes outline the area shown in Figs. 5.2 and 5.3, respectively. The station locations for Orlando International Airport (MCO) and buoy 41009 are given by the "M" and "9" symbols, respectively.

At 1600 UTC 7 June (Fig. 5.2a), a distinct line of clouds associated with the east coast sea breeze extends from Jacksonville (JAX) down to the southern tip of the state. A similar line of clouds associated with the west coast sea breeze extends northwest from Tampa (TBW) to the Big Bend area just south of Tallahassee (TLH). By 2000 UTC 7 June (Fig. 5.2b), the east and west coasts sea-breeze circulations propagate toward the center of the state. The cloud band associated with the west coast sea breeze along the southwest coast of Florida at 2000 UTC is not clearly evident 4 h earlier at 1600 UTC (compare Figs. 5.2a, b). As is common during the warm season afternoons in Florida, significant deep convection is occurring along sections of the sea breeze.

A meso-beta scale analysis of the sea breeze during 7 June in east-central Florida is shown by the streamlines of gridded wind observations from the KSC/CCAS tower network (Fig. 5.3). The 54-ft (16.5-m) level *u*- and *v*-component of the wind from the KSC/CCAS network at 5-minute intervals are analyzed to a 4-km grid using a two-pass Barnes (1964) scheme. From representative 4-km grid intervals shown in Fig. 5.3, it can be inferred that most of the KSC/CCAS tower network is contained within a single 29-km eta model grid box. Therefore, the meso-eta model is not expected to resolve any of the spatial variability in wind speed or direction that appears in Fig. 5.3. However, the observed wind tower data are useful to illustrate the movement of the sea-breeze front across KSC/CCAS (e.g. Laird et al. 1995).

Figure 5.2. The 4-km GOES visible imagery for (a) 1600 UTC 7 June 1996 and (b) 2000 UTC 7 June 1996. Station identifiers for Jacksonville, FL (JAX), Tampa Bay, FL (TBW) and Tallahassee, FL (TLH) are shown in panel (a).

The streamlines and 54-ft tower observations plotted in Fig. 5.3a show a light northwest or offshore flow at 1200 UTC 7 June. By 1400 UTC 7 June, the sea-breeze front moves to the west of KSC/CCAS (beyond the left edge of Fig. 5.3) as indicated by the northeast winds. In addition to the wind shift, coastal towers are indicating an increase in wind speed relative to those observed 2-h earlier. The tower data plotted in Fig. 5.3 demonstrate that the observed sea breeze forms and passes to the west of KSC/CCAS in less than two hours.

It is possible to estimate the onset time for the sea breeze across east-central Florida on 7 June by examining a time series of wind direction at 5-minute intervals averaged over all non-missing points in the 4-km analysis grid. As shown by the solid line in Fig. 5.4, the average wind direction veers markedly from about 330 to 60˚ between 1200 and 1300 UTC in association with the passage of the sea breeze across the KSC/CCAS region. Despite the fact that the observed time series shown in Fig. 5.4 represents grid-averaged wind directions from objectively analyzed tower data at 5-minute intervals, there is still a great deal of variability present. In comparison, the 29-km eta model forecast time series of wind direction at XMR shown by the dashed line in Fig. 5.4 does not contain the high frequency fluctuations that are present in the observations. These results underscore the point made in section 4, namely that verifying model forecasts at individual points (or stations) is a very stringent test of model capability since the observations contain scales of motion not resolved by the model. The details from the 29-km eta model forecast of the sea breeze for this case including the point forecast of wind direction are discussed in section 5.1.1.2.

Figure 5.3. Streamlines of gridded wind data and wind barbs from 54-ft (16.5-m) KSC/CCAS tower observations at (a) 1200 UTC 7 June 1996 and (b) 1400 UTC 7 June 1996. Wind speeds are given by barbs (open circle = calm, half barb = 5 kt, full barb = 10 kt). The 4-km grid interval used for the Barnes objective analysis of zonal (u) and meridional (v) wind components from KSC/CCAS 54-ft tower observations is shown in each panel.

5.1.1.2 29-km Eta Model Forecast of Sea Breeze Structure

The 29-km eta model run beginning 0300 UTC 7 June is used to depict the forecast evolution of the sea breeze in Figs. 5.5 and 5.6. The left column of Fig. 5.5 (panels a-d) shows 2-m temperature gradients and 900-mb vertical velocities while the right column (panels e-h) shows 10-m wind speed and direction and divergence of the 10-m wind u-component. The vertical cross sections of potential temperatures, vertical velocities, temperature gradients, and circulation vectors along the lines X-X'

in Fig. 5.5 are shown in Fig. 5.6. These quantities are displayed at 3-h intervals for the 12-h forecast period from 1500 UTC 7 June through 0000 UTC 8 June.

The meso-eta model depicts strong differential heating across the land/sea boundaries along the east and west coasts of Florida as temperatures are forecast to increase more rapidly over land than over water. The evolution of the forecast 2-m temperature gradient is shown by the shading in Fig. 5.5 (panels a-d) with darker shading indicating stronger temperature gradients. Note that shaded temperature gradients are shown in Fig. 5.5 because they provide more remarkable delineation of land-sea temperature contrasts than isotherms especially when animating the fields. For the purposes of qualitative verification, Table 5.1 lists the observed temperature at Orlando International Airport (MCO) and at buoy 41009 located approximately 50 km east of CCAS (see Fig. 5.1 for station locations). The forecast temperature gradient along the east coast is most pronounced around 2100 UTC 7 June (Fig. 5.5c) when the observed temperature difference of 6.6 ˚C between MCO and 41009 is largest (Table 5.1).

Figure 5.4. Time series of wind direction from 1100 to 2300 UTC 7 June 1996. The solid line shows wind direction at 5-minute intervals averaged over all non-missing points from the gridded analyses shown in Fig. 5.3. The dashed line represents the forecast wind direction at XMR from the 29-km eta model run beginning at 0300 UTC 7 June 1996. The point forecast data are available at 1-h intervals corresponding to the times indicated by the dots along the dashed line.

Figure 5.5. Evolution of the forecast sea breeze from the 29-km eta model run beginning 0300 UTC 7 June 1996. Panels a-d show 2-m temperature gradients (shaded every 1 x 10^{-2} K km^{-1}) and 900-mb vertical velocities (μb s^{-1}) while panels e-h show 10-m wind speed (kt) and direction and divergence of the 10-m wind *u*-component (x 10^{-5} s^{-1}). Charts are shown at 3-h intervals from 1500 UTC 7 June through 0000 UTC 8 June as labeled in each panel. 10-m wind speed is shaded at 5-kt intervals beginning at 5 kt. Solid (dashed) lines in panels a-d indicate upward (downward) motion with an isopleth interval of 2 μb s^{-1}. Solid (dashed) lines in panels e-h indicate convergence (divergence) with an isopleth interval of 2 x 10^{-5} s^{-1}. Lines X-X′ depict the location of vertical cross sections shown in Fig. 5.6. Note that the zero isopleth is omitted on all panels.

Figure 5.6. Vertical cross sections of potential temperature (K), vertical velocity (μb s^{-1}), temperature gradient (10^{-2} K km^{-1}), and circulation along lines X-X′ in Fig. 5.5. Potential temperature (K) is shown by the thick solid lines while shading shows the horizontal temperature gradient at each level. Positive or downward (negative or upward) vertical velocity are indicated by thin solid (dashed) lines. Arrows depict circulation in the plane of the cross section. The thick solid lines at the bottom of each cross section approximate the location of land along the lines X-X′. The isopleth interval is 1 K for potential temperature and 1 μb s^{-1} for vertical velocity.

Table 5.1. Observed 2-m temperatures (˚C) and temperature difference (ΔT) between MCO and buoy 41009 for 7 to 8 June 1996.

Time (UTC) / Date	Orlando International Airport (MCO)	buoy 41009	ΔT (MCO-41009)
1500 / 7 June	29.4	26.7	2.7
1800 / 7 June	32.8	26.7	6.1
2100 / 7 June	33.3	26.7	6.6
0000 / 8 June	28.9	26.7	2.2

In conjunction with the developing temperature gradients shown in Fig. 5.5, the meso-eta forecasts a transition in the 10-m wind field that is consistent with the onset of the observed sea breeze along Florida's east and west coast. Between 1200 UTC 7 June and 1500 UTC 7 June 1996, the model forecast winds along Florida's north-central east coast shift from an offshore direction (not shown) to a north-northeasterly onshore direction (Fig. 5.5e). The forecast 10-m winds continue to veer from north-northeast at 1500 UTC 7 June to east by 0000 UTC 8 June, especially along the northern section of the east coast (Fig. 5.5e-g). A more dramatic shift in direction occurs along the west coast where weak east-southeast winds at 1500 UTC 7 June veer by more than 250˚ and become northwesterly by 0000 UTC 8 June as the model forecasts a west coast sea breeze (Figs. 5.5e-h).

The time series of forecast wind direction at 1-h intervals from XMR (Fig. 5.4) confirms that the model veers the wind along the east coast from about 320 to 70˚ between 1100 and 2300 UTC 7 June. The 1-h forecast wind directions are in good agreement with the analyzed, grid-averaged wind directions derived from the 5-minute, KSC/CCAS tower observations (Fig. 5.4). From the 5-minute temporal resolution of the tower data, it is possible to determine that the onset of the observed east coast sea breeze occurs between 1200 and 1400 UTC 7 June as the winds veer from 330 to 60˚ (Fig. 5.4). Although the 29-km eta model exhibits a similar but more gradual shift in wind direction between 1100 and 1500 UTC 7 June, the forecast winds for this case also veer in agreement with the shift of observed winds shown in Fig. 5.4.

The changes in wind direction associated with the forecast sea breeze are also accompanied by an increase in wind speed. The 10-m wind speeds (shading in Figs. 5.5e-h) increase along both coasts especially between 1800 and 2100 UTC 7 June. In fact, there is a marked increase in 10-m wind speed forecast along the northeast coast as shown by the darker shaded area (speed ≥ 10 kt) moving from east of the Florida-Georgia border at 1800 UTC to the northeast coast of Florida by 2100 UTC 7 June (Figs. 5.5f, g). Such changes in 29-km eta model 10-m wind speed are useful for identifying the occurrence of forecast sea breezes even in cases where the prevailing synoptic flow is already onshore. In these cases, there is no distinct shift in wind direction from offshore to onshore flow associated with the onset of the sea breeze. However, the winds still accelerate as the pressure gradient strengthens in response to stronger heating over land. The forecast evolution of wind speed and direction shown in Fig. 5.5 is in general agreement with standard land and buoy surface observations (not shown) that confirm the formation of a sea breeze along the east and west coast of Florida on 7 June.

Figure 5.5 shows that the transition to onshore wind flow along both coasts enhances low-level convergence and vertical motion, reflecting the development of a thermally-direct circulation over the Florida peninsula. These patterns are shown in Fig. 5.5 by the convergence of the u-component of the 10-m wind (panels e-h) and the 900-mb vertical velocities (panels a-d). Note that the convergence of the zonal wind (u) rather than total wind is used in order to highlight convergent flows which result from changes in wind speed and direction perpendicular to the coastlines. The magnitude of the 10-m zonal wind convergence and negative (upward) 900-mb vertical motions increase markedly from 1500 through 2100 UTC 7 June. The convergence of the 10-m zonal wind exceeds 7×10^{-5} s^{-1} at 2100 UTC along the northeast coast of Florida (Fig. 5.5g). In addition, the largest maximum upward motions on the order of -7 μb s^{-1} at 900 mb are forecast over the same area at 2100 UTC 7 June.

The vertical cross sections along the lines X-X′ in Fig. 5.5 (a-d) further illustrate the horizontal scale and vertical extent of thermally-direct circulation forecast by the meso-eta model on 7 June. The thick solid line at the bottom of each panel in Fig. 5.6 approximates the location of land along the lines X-X′. The potential temperatures (K) and shading in Fig. 5.6 show that the 29-km eta model forecasts strong temperature gradients below 900 mb along both coasts which is maximized around 2100 UTC 7 June (Fig. 5.6). The circulation vectors imply low-level convergence especially along the

west coast as the winds below 900 mb shift from offshore to onshore by 1800 UTC 7 June. The isopleths of forecast vertical motion depict rising motion exceeding -5 μb s^{-1} between 975 and 850 mb at 0000 UTC 8 June. The core of maximum upward motion occurs over land between 2100 UTC 7 June and 0000 UTC 8 June with subsidence found offshore along both coasts of Florida (Fig. 5.6). The thermally-direct circulation depicted in Fig. 5.6 extends through the lowest 3 km of the model atmosphere. The vertical extent of the forecast sea breeze is significantly higher than the 1-2 km observed at different mid-latitude and tropical locations around the world (Atkinson 1981, pp. 144-145). Local measurements from the KSC Atmospheric Boundary Layer Experiment show the average depth of the observed sea breeze at KSC/CCAS to be on the order of 600 to 800 m (Taylor et al. 1990).

As described in the subjective evaluation protocol (section 3), the KSC/CCAS network of 915-MHz wind profilers was to be used for verifying the vertical extent of the sea breeze along the central east coast of Florida. However, the 915-MHz profiler data were not available until well after the warm season evaluation period ended. As a result, these data can not be used to compare the depth of the observed and forecast sea breezes. The evaluation protocol also called for the sea-breeze analysis to verify the propagation of the east and west coast sea breeze as inferred from the movement of cloud bands shown in Fig. 5.2. This portion of the analysis is not performed primarily because the 29-km eta model does not resolve the meso-beta scale structure of the observed sea breeze detailed by the cloud patterns and wind fields in Figs. 5.2 and 5.3, respectively.

5.1.2 Verification of Sea-Breeze Occurrence

The case example from 7 June 1996 demonstrates that the 29-km eta model can forecast a sea breeze that is characterized by a peninsula-scale, thermally-direct circulation. The following analysis focuses on determining the skill of the meso-eta model in forecasting the occurrence of an east or west coast sea breeze anywhere along the Florida peninsula during the entire warm season (May through August 1996). As detailed in section 5.2, the meso-eta model's ability to represent accurately the occurrence of convection over Florida is closely related to the forecast sea-breeze circulation documented in this section.

The initial step in the sea-breeze verification is to count the occurrence of forecast and observed east and west coast sea breezes. The verification is performed for all days during the warm season when (1) both observations and 29-km eta model forecasts are available and (2) either the east or west coast of Florida is not affected by tropical waves, tropical cyclones, or fronts. The occurrence of observed sea breezes is determined subjectively using the 4-km GOES visible imagery as shown in Fig. 5.2. The visible satellite images at 1-h intervals from 1200 through 2300 UTC are animated to determine if narrow cloud bands similar to those shown in Fig. 5.2 form along either coast during the 11-h verification period. As shown in Figs. 5.3 and 5.4, wind analyses from KSC/CCAS tower data are also useful to identify the onset of the sea breeze along the central east coast of Florida. However, these analyses depict only the meso-beta scale aspects of the observed sea breeze over a small fraction of Florida's east coast. Therefore, the 4-km gridded fields of KSC/CCAS tower wind speed and direction are animated to confirm the onset of the east coast sea breeze only in cases when the 4-km satellite data indicate a sea-breeze event based on cloud patterns.

Alternatively, it is possible to use Doppler radar data to detect sea breezes and other circulations such as horizontal convective rolls as discussed by Weckworth et al (1997). It would be necessary to obtain and examine data for the entire warm season from several NEXRAD sites in order to identify the occurrence of east and west coast sea breezes along any portion of the Florida peninsula. In terms of time and resources, such extensive radar data analysis is beyond the scope of the present study. Therefore, verification of the observed sea breezes along both coasts of Florida is based primarily on cloud signatures shown by the 4-km visible GOES imagery.

There are several limitations with using shallow cloud bands to identify the occurrence of east or west coast sea breezes. First, as pointed out earlier in this section, it is likely that sea breeze circulations are present prior to the appearance of visible cloud bands. However, the cloud features are only used to determine the occurrence rather the actual location and motion of the sea breeze. Second, shallow cumulus cloud bands can be obscured by anvil debris or other high-level clouds. On some days during the warm season, a wind shift is observed in the KSC/CCAS tower network consistent with the onset of a east coast sea breeze but there is insufficient moisture present in the atmosphere to form clouds. These few days are excluded from the analysis since the verification focuses on the occurrence of east coast sea-breeze events over much broader areas not covered by the KSC/CCAS tower network.

The occurrence of forecast sea breezes is determined by animating meso-eta gridded fields similar to those shown in Figs. 5.5 and 5.6 at 3-h intervals from all available 0300 UTC model runs. These fields include 2-m temperature gradients, changes in 10-m wind speed and direction, low-level convergence and vertical motion patterns, and thermally direct circulations. For the purpose of verification, a forecast east or west coast sea breeze is identified when the sequence of 3-h model output shows a shift in wind direction from offshore to onshore flow and/or an increase in wind speed along either coast in combination with the other thermodynamic and kinematic features that appear in Figs. 5.5 and 5.6.

The meso-eta model does not have sufficient horizontal resolution to resolve the individual circulations associated with the east and west coast sea breezes. Nevertheless, the model is capable of forecasting changes in low-level wind speed and direction that are consistent with the onset of the sea breeze along either coast as illustrated in Fig. 5.5. In fact, there are a number of warm season cases when the model forecasts only an east or west coast sea breeze. Therefore, the analysis considers separate verification of east and west coast events. The verification does not include sea-breeze forecasts from 1500 UTC model runs because these gridded data were not archived as part of the overall 29-km eta model evaluation.

As shown later in section 5.2, the 29-km eta model often produces low-level convergence and thermally direct circulations that are not related to the formation of a sea breeze. Other days are characterized by synoptic-scale or mesoscale onshore flow that is not associated with sea-breeze circulations and the model forecasts low-level speed convergence as onshore winds decrease due to stronger friction over land. For these reasons, forecast sea breezes are more likely to verify correctly when the temperature gradients and other characteristic patterns illustrated in Figs. 5.5 and 5.6 are present together and oriented nearly parallel to the coast. In conjunction with the gridded model fields, the point or station forecasts at XMR and TBW are also used to detect and/or confirm changes in wind speed and direction associated with the onset of forecast sea breeze along the east and west coast, respectively.

The occurrence of forecast and observed east and west coast sea breezes as determined from available warm season data are counted and entered in a four-cell contingency table shown in Table 5.2. The data from the contingency table are then used to compute the bias, false alarm rate (FAR), and probability of detection (POD), critical success index (CSI), and Heidke skill score (HSS) for east and west coast sea-breeze events. The definitions of the bias, FAR, POD, CSI, and HSS are given in Table 5.2 and follow Schaefer (1990) and Doswell et al. (1990).

Table 5.2. Example of four-cell contingency table used for verification of sea-breeze occurrence and definitions of verification scores.

		Observed Sea Breeze	
		Yes	No
Forecast Sea Breeze	Yes	W	X
	No	Y	Z

$$N = W + X + Y + Z$$

$$bias = (W + X) / (W + Y)$$

$$\text{false alarm rate (FAR)} = X / (W + X)$$

$$\text{probability of detection (POD)} = W / (W + Y)$$

$$\text{critical success index (CSI)} = W / (W + X + Y)$$

$$\text{Heidke skill score (HSS)} = [(W + Z) - E] / (N - E)$$

$$E = [(W + Y)(W + X) + (X + Z)(Y + Z)] / N$$

The number of forecast and observed east and west coast sea-breeze events and summary statistics are presented in Table 5.3. The number of verification days (N=70) is less than the total number of days (123) during the warm season evaluation period as a result of missing forecast and/or observational data. The bias of 0.63 and POD of 0.56 for east coast events reveals that the meso-eta model forecasts the occurrence of the east coast sea breeze just slightly more than 50% of the time it is observed. The bias of 0.48 and POD of 0.38 is smaller for west coast than for east coast events and indicates that the model underestimates the occurrence of the west coast sea breeze. These differences in forecast accuracy between the east and west coast sea-breezes are also reflected by the CSI and HSS. For random forecasts the HSS is equal to zero. Therefore, although more accurate along the east coast, the model does provide an improvement over random forecasts for the occurrence of sea-breezes along both coasts. Finally, the relatively low FAR between 0.10-0.20 suggest that the model does not often forecast sea breezes which are not observed.

Table 5.3. East and west coast sea-breeze events and summary statistics.

East Coast Sea Breeze Events						
		Observed		Bias	=	0.63
		Yes	No	FAR	=	0.11
Forecast	Yes	24	3	POD	=	0.56
	No	19	24	CSI	=	0.52
				HSS	=	0.40
West Coast Sea Breeze Events						
		Observed		Bias	=	0.48
		Yes	No	FAR	=	0.20
Forecast	Yes	16	4	POD	=	0.38
	No	26	24	CSI	=	0.34
				HSS	=	0.21

There are likely a number of reasons why the 29-km eta model correctly forecasts only slightly more than half of observed east and west coast sea breeze events along the Florida peninsula. Experience from the AMU warm season forecast exercises suggests that the model typically does not forecast the occurrence of observed sea breezes on days characterized by larger-scale forecast errors over a significant portion of Florida. For example, the model run beginning at 0300 UTC 18 June 1996 forecasts Tropical Storm Arthur in the western Atlantic to make landfall north of Daytona Beach, FL. As a result, the forecast is dominated by the circulation associated with Arthur rather than the characteristic patterns of forecast sea breezes shown in Figs. 5.5 and 5.6. However, Arthur tracked more northwesterly and made landfall in South Carolina. While the storm remained to the northeast of the peninsula on 18 June, 4-km visible GOES imagery clearly shows the formation of well-defined sea breezes along the east and west coasts of Florida (not shown).

In concluding this section on sea-breeze verification, it is worth noting that 29-km eta model forecasts of Florida sea breezes may be of limited utility for the following reasons.

- The model only resolves the larger-scale aspects of the observed sea-breeze as demonstrated by the peninsula-scale, thermally-direct circulation shown in Fig. 5.6.

- The model runs beginning at 0300 UTC correctly forecast about 50% of the observed east and west coast sea breezes.

An interesting extension of the sea breeze analysis would be to determine whether model runs initialized 12-h later at 1500 UTC provide more accurate forecasts of sea breeze occurrence. However, guidance from 1500 UTC model runs is typically available well after the onset of east or west coast Florida sea breezes.

5.2 Thunderstorm Verification

Warm season thunderstorms in Florida result primarily from interactions between mesoscale phenomena. Because larger-scale models commonly used in operations (i.e., NGM, 48-km eta) cannot resolve the spatial and temporal details of these phenomena, forecasters must utilize observations and persistence to develop accurate short-term (< 6 h) thunderstorm forecasts. Given its 29-km grid point resolution, the meso-eta model is not expected to resolve features such as individual convective cells or thunderstorm outflow boundaries. Although thunderstorms are not explicitly forecast by the model, basic diagnostic quantities from its 3-h grid (1-h point) output provide utility by allowing users to follow trends and make inferences about the environments which may be conducive for thunderstorm development. In order to demonstrate this utility, examples of thunderstorm development and verification of warm season precipitation are presented in the following sections.

5.2.1 Case Examples

The examples presented here are analyses of observed and forecast thunderstorm development on 1 to 2 August 1996 (case 1) and 9 to 10 August 1996 (case 2). The first case represents a day when the 0300 UTC meso-eta run adequately forecasted several features important for afternoon thunderstorm development. These features include surface temperature gradients associated with heating in clear versus cloudy areas and low-level wind convergence associated with a developing thermal trough. The example from 1 to 2 August presents a best-case scenario since the meso-eta model did not forecast the evolution of convection as well for other cases during the warm season.

Case 2 is chosen to illustrate an alternate scenario for a day when the model produces a much less accurate forecast of convection across Florida.

5.2.1.1 Forecast and Observed Convection

The evolution of forecast and observed convection for cases 1 and 2 are compared using satellite imagery and forecast precipitation. Throughout the following discussion, areas of colder cloud tops and strong gradients in cloud top temperatures on the 4-km IR satellite images are used as a proxy for observed precipitation. The satellite images are chosen at times near the mid-point of the 3-h periods over which model precipitation is accumulated. The occurrence of forecast thunderstorms is based on total precipitation from 0300 UTC model runs which is accumulated and output on the 40-km AWIPS grid every 3 h. The model's total precipitation includes contributions from the convective parameterization (Betts and Miller 1986; Janjic 1994) and from the explicit cloud prediction scheme (Zhao et al. 1997) that diagnoses rain as part of the cloud microphysics. Similar to sea-breeze verification, thunderstorm verification is performed using 0300 UTC rather than 1500 UTC model runs.

A snapshot of the observed and modeled evolution of the events on 1 to 2 August 1996 is depicted in Figs. 5.7a-c. The IR satellite imagery at 1915 UTC 1 August (Fig. 5.7a) suggests that scattered shower activity is present over northern Florida. At the same time, thunderstorms are evident along the east coast sea breeze in southern Florida with fewer clouds over central Florida. The forecast precipitation between 1800 and 2100 UTC 1 August appears excessive in northern Florida since the 0.25" isopleth covers about one-half of the Florida panhandle (Fig. 5.7a). Nevertheless, examination of IR satellite images at 1815 and 2015 UTC 1 August (not shown) reveals that at different times within the 3-h forecast period, transient, scattered showers cover the area within the 0.10" forecast precipitation isopleth. In this regard, the spatial distribution of observed precipitation over northern Florida is forecast reasonably well by the model. In other areas, the model adequately forecasts the spatial coverage of the developing thunderstorms over southeastern Florida while an absence of forecasted precipitation is noted over east-central Florida (Fig. 5.7a).

There is one important feature on the 1915 UTC 1 August IR satellite image (Fig. 5.7a) which is *not* forecast by the meso-eta model. The small, bright area to the northwest of Cape Canaveral, FL reveals that a thunderstorm is present in the area. Surface weather observations from XMR confirm the presence of thunderstorms which produce a 40-kt wind gust at 1819 UTC (Table 5.4). In fact, there are a number of other instances throughout the warm season evaluation period when the meso-eta model fails to predict the spatial and temporal evolution of individual thunderstorms that produce significant weather.

Table 5.4. Surface weather observations at XMR for 1 August 1996.

Time (UTC)	Wind Direction/ Speed (kt)	Weather	Time (UTC)	Wind Direction/ Speed (kt)	Weather
1655	210/08	VCSH	1855	90/06	TSRA
1755	260/07	TS	1914	100/02	TS
1819	250/07G40	TS	1955	210/04	TS
1833	120/09	TSRA	2039	150/03	---

VC = In the Vicinity; SH = Showers; TS = Thunderstorm; RA = Rain

At 2215 UTC 1 August, the large area of colder cloud tops in Fig. 5.7b indicates that thunderstorms are present across central Florida along a southwest-northeast oriented line. Smaller storms continue over the northern and southwestern parts of Florida. Subsequent satellite images indicate that convection is still active 3 h later at 0115 UTC (Fig. 5.7c). The meso-eta model precipitation shown in Figs. 5.7b, c indicates that the location and spatial extent of the convection

over central Florida are forecast remarkably well by the model between 1800 UTC 1 August and 0300 UTC 2 August. As with the previous 3-h period from 1800 to 2100 UTC (Fig. 5.7a), forecast precipitation amounts over northern Florida between 0000 and 0300 UTC are still likely high in

Figure 5.7. The 4-km GOES infrared imagery for case 1 (1 to 2 August 1996) and case 2 (9 to 10 August 1996) at times shown in each panel. Meso-eta model forecast precipitation for 3-h periods

from 1800 to 2100 UTC (panels a, d), 2100 to 0000 UTC (panels b, e), and 0000 to 0300 UTC (panels c, f) is shown by the solid lines in each panel. Precipitation amounts are contoured at 0.01, 0.10, 0.25, and 0.50".

comparison with observed rainfall from inferred from areas of convection depicted on the IR satellite image (Fig. 5.7b).

The sequence of IR satellite images and model precipitation for the second thunderstorm case example on 9 to 10 August 1996 is shown in Figs. 5.7d-f. At 1915 UTC 9 August, the primary areas of observed convection are found over the Gulf of Mexico, Florida panhandle, south Florida, and over the Straits of Florida extending northeast to the northern Bahama islands (Fig. 5.7d). The 3-h accumulated model precipitation from 1800 to 2100 UTC shows the 0.01" isopleth covering the areas of active convection over south Florida and the Florida panhandle. In addition, heavier amounts exceeding 0.10" are forecast in agreement with the broader area of convection oriented southwest-northeast in the Straits of Florida (Fig. 5.7d). Except for failing to produce precipitation in association with observed convection over the Gulf of Mexico, the model is generating a reasonably accurate depiction of the weather at 1915 UTC 9 August. Indeed, the model does not generate precipitation over the northern and central parts of the Florida peninsula where skies remain generally cloud free.

By 2215 UTC 9 August, observed convective activity increases over the Florida panhandle and south Florida while it decreases over the Straits of Florida (Fig. 5.7e). The model continues to forecast light amounts of precipitation over these same areas as shown by the 0.01" isopleth in Fig. 5.7e. The model also develops an extensive area of precipitation along most of Florida's east coast that extends into south Georgia with amounts exceeding 0.10" over central east Florida between 2100 UTC 9 and 0000 UTC 10 August (Fig. 5.7e). This forecast precipitation does not coincide with any observed convection at 2215 UTC except the area along the southeast coast to the east of Lake Okeechobee. At this point, the model forecast is beginning to diverge from the evolution of events in the real atmosphere.

In the subsequent 3-h period, the IR image for 0115 UTC 10 August (Fig. 5.7f) reveals that the cold cloud tops expand dramatically in the Florida panhandle with smaller areas of convection still present in south central Florida. The 3-h accumulated precipitation forecast by the model from 0000 to 0300 UTC 10 August remains light across the Florida panhandle. However, both the spatial coverage and amount of precipitation along the east coast increase significantly from the previous 3-h period with totals exceeding 0.25" over the eastern half of the peninsula north of Lake Okeechobee (Fig. 5.7f). The forecast precipitation from 0000 to 0300 UTC 10 August is erroneous over the central and eastern portions of the peninsula since few significant cold cloud tops are evident from the satellite imagery in that area at 0115 UTC 10 August (Fig. 5.7f).

In general, the model's 3-h accumulated forecast precipitation for both cases provides a reasonably accurate depiction of the broad-scale areas of observed convection from 1800 to 2100 UTC over the domain shown in Fig. 5.7. However, the accuracy of meso-eta precipitation forecasts after 2100 UTC (1700 EDT) for each case is quite different as discussed in the preceding paragraphs. Whereas case 1 depicts a remarkably accurate forecast of developing convection, case 2 represents a forecast of excessive precipitation. By exploring differences between these two cases in greater detail, lessons may be learned about the meso-eta model's capabilities and limitations in forecasting convection. Throughout the AMU's warm season forecasting exercise, it was determined that animation of the 3-h gridded model output provides additional value by helping to identify features that become important for developing convection. A limited number of model fields from these animations are shown in subsequent figures to compare other features of the meso-eta model runs that may affect the accuracy of precipitation forecasts for these cases.

5.2.1.2 Forecast 2-m Temperature, 10-m Wind, Vertical Cross Sections

The 18-h, 21-h, and 24-h forecast 2-m temperatures and 10-m winds at 2100 UTC, 0000 UTC, and 0300 UTC, respectively along with surface temperature and wind observations are shown for both cases in Fig. 5.8. In addition, vertical cross sections of potential temperatures, vertical velocities, temperature gradients, and circulation vectors along the lines X-X′ and Y-Y′ in Fig. 5.8 are depicted in Fig. 5.9. These parameters are very similar to those shown for the sea breeze verification as they are designed to illustrate the development and vertical extent of thermally-direct circulations produced by the model on 1 to 2 August and 9 to 10 August 1996.

Forecast 2-m temperatures (˚C) at 2100 UTC 1 August indicate that central Florida is warmer than surrounding land areas to the north and south (see shading in Fig. 5.8a). The forecast temperature gradient between warmer and cooler areas likely resulted from differential heating between the relatively cloud-free area over central Florida and the cloudy regions in the northern and southern sections of the peninsula. Corresponding surface temperature observations (˚C) are plotted as small numbers in Fig. 5.8a and corroborate the forecast temperature distribution. As forecast surface temperatures exceed 31 ˚C, a thermal trough (not shown) develops in the surface pressure field in an orientation perpendicular to line X-X′. Streamlines of the forecast 10-m winds suggest a southwest-northeast line of low-level convergence associated with the developing thermal trough (Fig. 5.8a). The forecast streamlines in Fig. 5.8a clearly illustrate the onshore flow and convergence associated with the thermal trough although they do not exactly match the observed wind directions shown by the wind barbs plotted in Fig. 5.8a.

By 0000 UTC 2 August, the forecast 2-m temperature gradient weakens as cooling begins to occur over land areas near sunset. Surface temperature observations plotted in Fig. 5.8b confirm this forecast trend, particularly over central Florida where decreases in temperatures are greatest. However, the low-level convergence zone oriented southwest-northeast across the peninsula is still well-defined by the forecast 10-m streamlines at this time. Here again the low-level flow pattern is in general agreement with the observed winds although discrepancies exist especially at coastal stations in south Florida (Fig. 5.8b). The 2-m temperature gradient continues to weaken across Florida at 0300 UTC 2 August and is primarily found along the coastline as the land areas cool faster than the adjacent water bodies. The observed surface temperatures at this time range from 24 to 25 ˚C in central Florida and also indicate a very weak temperature gradient from north to south across the region (Fig. 5.8c). The convergence in forecast 10-m winds at 0000 UTC 2 August across central Florida is replaced by a general southeast flow at 0300 UTC 2 August that becomes more southerly to southwesterly over northern sections of the state. The model forecasts the larger-scale aspects of the 10-m wind field quite well at 0300 UTC 2 August although there are still some substantial local differences compared with the observed wind directions shown in Fig. 5.8c.

The sequence of forecast and observed 2-m temperatures and 10-m streamlines for 2100 UTC 9 August to 0300 UTC 10 August (case 2) is shown in Figs. 5.8d-f. As with case 1, the strongest thermal contrast between land and the surrounding waters occurs at 2100 UTC and decreases with time as daylight hours end. As the temperature contrast intensifies, the model forecasts the development of a thermal trough (not shown) and associated area of convergence that is indicated by the 10-m streamlines in Figs. 5.8d-f. This low-level convergence zone slowly propagates westward from the east coast of Florida at 2100 UTC 9 August to the center part of the peninsula by 0300 UTC 10 August. For the most part, the forecast patterns of low-level temperature and wind patterns from 2100 UTC 9 to 0300 UTC 10 August are supported by the surface temperature and wind observations plotted in Figs. 5.8d-f. The forecast temperatures and streamlines shown in Fig. 5.8 reveal that both cases develop low-level convergence zones which are supported by observations. It is useful to

examine vertical cross sections in order to compare the strength of circulations that form in response to the low-level convergence.

Figure 5.8. Meso-eta model forecasts of 2-m temperature (shading in ˚C) and 10-m wind streamlines for case 1 (1 to 2 August 1996) and case 2 (9 to 10 August 1996) at times shown in each panel. Corresponding surface temperature (˚C) and wind (kt) observations are plotted using standard convention. Lines X-X′ and Y-Y′ depict the location of vertical cross sections shown in Fig. 5.9.

Vertical cross sections for case 1 along the lines X-X′ in Figs. 5.8a-c are shown in Figs. 5.9a-c. The forecast potential temperature (K) and shading of the temperature gradient in the model highlight the fact that the strongest thermal contrast occurs at 2100 UTC 1 August over central Florida in the lowest model layers below 900 mb (Fig. 5.9a). In addition, the shading around 700 to 600 mb in Fig. 5.9a suggests the presence of a lower tropospheric temperature inversion. The circulation vectors in Fig. 5.9a imply low-level convergence. The isopleths of vertical motion show rising motion over the center of the surface convergence zone and area of maximum heating while subsidence occurs on either side. The maximum upward motion on the order of -4 $\mu b\ s^{-1}$ at 2100 UTC 1 August is centered around 850 mb (Fig. 5.9a).

By 0000 UTC 1 August, the low-level temperature gradients are more diffuse (Fig. 5.9b) which is consistent with the decrease in 2-m temperatures shown in Fig. 5.8b. However, the vertical velocities increase from -4 $\mu b\ s^{-1}$ at 2100 UTC 1 August to -6 $\mu b\ s^{-1}$. As upward motion extends above 500 mb the weak temperature inversion evident at 2100 UTC between 600 and 700 mb (shading in Fig. 5.9a) is not present across the entire cross section at 0000 UTC 1 August (Fig. 5.9b). At 0300 UTC 2 August, the low-level thermal gradients continue to weaken but the vertical velocities increase to more than -7 $\mu b\ s^{-1}$ between 750 to 650 mb (Fig. 5.9c). The patterns of horizontal and vertical motion for case 1 (Figs. 5.9a-c) depict a thermally-direct circulation which is likely enhanced in response to developing forecast precipitation across central Florida after 2100 UTC 1 August (Figs. 5.7b, c).

The vertical cross sections for case 2 also show the development of a thermally-direct circulation (Figs. 5.9d-f). As with case 1, the most-pronounced low-level temperature gradients occur at 2100 UTC. In fact, the thermal gradients in the lower troposphere and those associated with the temperature inversion around 650 mb are stronger for case 2 than for case 1. A comparison of vertical velocities in Figs. 5.9b and 5.9e clearly shows that upward motions at 0000 UTC are also stronger for case 2 than for case 1. However, this trend does not continue at 0300 UTC as the maximum rising motion for both cases is on the order of -7 $\mu b\ s^{-1}$ around 700 mb.

5.2.1.3 Forecast and Observed Sounding Parameters

Examination of the precipitable water (PWAT) and convective available potential energy (CAPE) from forecast and observed soundings at XMR and TBW are shown to illustrate differences between the moisture and stability for cases 1 and 2 that may indirectly contribute to the aforementioned strength of the vertical circulations. Although forecast soundings at XMR and TBW are available every hour, stability parameters are only compared for those times listed in Table 5.5 when corresponding observed soundings are available. Note that the 2200 UTC soundings correspond to the time when forecast precipitation develops near XMR in both cases as shown in Figs. 5.7b, e. For case 1, the model underestimates the CAPE at all times for both stations which is consistent with the negative bias in CAPE identified during the entire warm season (Table 4.1; section 4.3). At TBW, the forecasts of PWAT agree very well with observed values. However, forecasts soundings at XMR are too dry as indicated by the smaller PWAT compared with the observed values in Table 5.5.

Figure 5.9. Vertical cross sections of potential temperature (K), vertical velocity, temperature gradient, and circulation along lines X-X′ and Y-Y′ in Fig. 5.8. Potential temperature (K) is shown by the thick solid lines while shading emphasizes the horizontal temperature gradient at each level (x 10^{-2} K km^{-1}). Positive or downward (negative or upward) vertical velocity (μb s^{-1}) are indicated by thin solid (dashed) lines. Arrows depict circulation in the plane of the cross section. The isopleth interval is 1 K for potential temperature and 1 μb s^{-1} for vertical velocity. The temperature gradients are shaded every 1 x 10^{-2} K km^{-1}.

Table 5.5. Precipitable water (PWAT; mm) and convective available potential energy (CAPE; J kg^{-1}) derived from forecast (FCST) and observed (OBS) soundings at XMR and TBW for 1 to 2 August 1996 and 9 to 10 August 1996. Dashes denote missing data.

		XMR (Case 1)						XMR (Case 2)			
	Time	PWAT		CAPE			Time	PWAT		CAPE	
Date	(UTC)	FCST	OBS	FCST	OBS	Date	(UTC)	FCST	OBS	FCST	OBS
1 Aug	1000	41	47	13	2070	9 Aug	1000	40	40	255	1353
1 Aug	2200	50	54	1446	1493	9 Aug	2200	50	44	1916	1232
2 Aug	1000	49	---	1	---	10 Aug	1000	41	38	2	2025
		TBW (Case 1)						TBW (Case 2)			
	Time	PWAT		CAPE			Time	PWAT		CAPE	
Date	(UTC)	FCST	OBS	FCST	OBS	Date	(UTC)	FCST	OBS	FCST	OBS
1 Aug	1200	47	47	158	1007	9 Aug	1200	46	52	54	1042
2 Aug	0000	48	48	736	2134	10 Aug	0000	45	50	1660	1754
2 Aug	1200	49	---	85	---	10 Aug	1200	49	47	21	1897

The examination of forecast and observed CAPE and PWAT for case 2 indicates similar differences with one very important exception. At XMR, the forecast sounding at 2200 UTC is actually too moist with a PWAT of 50 mm compared with the observed value of 44 mm. In addition, the forecast CAPE of 1916 J kg^{-1} is more than 50% larger than the observed value of 1232 J kg^{-1} (shaded row in Table 5.5). Since available upper air observations over the peninsula are sparse, it is difficult to determine if similar errors in PWAT and CAPE are present over broader regions along the northeast coast of Florida where forecast precipitation for case 2 appears excessive after 2100 UTC 9 August (section 5.2.1.1). Nevertheless, excess moisture and instability present in the forecast sounding at XMR is probably sufficient to trigger the convective parameterization and eventually produce precipitation.

5.2.1.4 Case Summary

In summary, there are similarities and differences between the model forecasts for cases 1 and 2. First, the 2-m temperature gradient and 10-m convergence zone for case 2 are oriented parallel to the coast and result from differential low-level heating across the land/sea interface. In fact, the thermally-direct circulation identified on 9 to 10 August is nearly identical to that shown for the case example of the forecast sea breeze in section 5.1. This result is not surprising since the overall warm season sea-breeze verification indicates that the model correctly forecasts the occurrence of an east coast sea breeze on 9 August 1996. In contrast, the low-level thermal and convergence patterns in case 1 likely form in response to differential heating between clear versus cloudy regions (Fig. 5.7a). Although the model correctly forecasts the occurrence of an east coast sea breeze for this case as well, the thermally-direct circulation for 1 to 2 August is not directly associated with the formation of a sea breeze.

A thermally-direct circulation is forecast by the model for both cases. In fact, the low-level temperature and convergence patterns identified in association with these circulations are found for numerous warm season cases. On some days such as 1 to 2 August 1996 (case 1), forecast precipitation coincides reasonably well with observed patterns of convection. On other days, the model overestimates the coverage and amount of convective precipitation as shown for 9 to 10 August 1996 (case 2). During the warm season, the PWAT and CAPE biases (Table 4.1) suggest that, on average, forecast soundings are too dry and too stable. In contrast, the model soundings for case 2 at XMR are too moist and unstable just prior to the onset of forecast precipitation over the northeast portion of the Florida peninsula. Both surface observations at XMR (not shown) and IR satellite data indicate that this forecast precipitation is erroneous.

It is possible that inaccurate precipitation forecasts for case 2 result from excessive moisture and instability documented in the forecast sounding at XMR. It would be useful to determine why the model overestimates the moisture and instability for case 2 when similar errors are not apparent for case 1. One plausible explanation is that too much Atlantic moisture is transported into the region by the low-level convergent flow associated with the thermally-direct circulation. Furthermore, errors in moisture flux could be related to inaccurate forecasts of wind speed and direction and moisture. It is apparent that more detailed diagnostics of model output and additional observations are required to explain differences in convection forecasts between cases such as those described in this section. A logical extension of the thunderstorm verification would be to examine more warm season cases to determine if errors similar to those discussed for case 2 affect the model's convective forecasts. Although such an analysis is beyond the scope of the current evaluation, it would likely help model users to understand more thoroughly the capabilities and limitations of warm season, meso-eta model precipitation forecasts over Florida.

5.2.2 Verification of Precipitation Occurrence

The case example from 1 to 2 August 1996 demonstrates that the meso-eta model occasionally has some utility in forecasting thunderstorms over Florida. However, there are a number of forecasts during the warm season that were much less accurate as shown for the case from 9 to 10 August 1996. The following analysis focuses on the skill of the model in forecasting thunderstorms over regions of the Florida peninsula during the entire warm season (May to September 1996).

5.2.2.1 Methodology

There are several steps involved in the verification of precipitation occurrence. First, the state is divided into six verification zones shown in Fig. 5.10. The motivation for bisecting the state from north to south is to determine if the meso-eta model could forecast distinct areas of convection associated with the east and/or west coast Florida sea-breeze circulations. The remaining divisions along the 27 and 29˚ latitude lines are subjective and result in six zones of roughly equal area (not counting the western most area of the panhandle). It is interesting to note that the width of each zone over land is approximately 120 km. Since the 29-km eta model can only resolve features with wavelengths on the order $4\Delta x$ or 116 km, the zone width corresponds well with the model's smallest resolvable wavelength.

Figure 5.10. Map of Florida showing definition of precipitation verification zones. See text for details.

The next step in the precipitation verification is to count the occurrence of forecast and observed precipitation over land in each zone during 3-h periods from 1500 to 1800 UTC, 1800 to 2100 UTC, and 2100 to 0000 UTC. These time periods are chosen to verify the forecast occurrence of thunderstorms during the 9 h from 1100 to 2000 EDT (1500 to 0000 UTC) when convection is most often observed in Florida during the warm season. The occurrence of forecast thunderstorms is determined using meso-eta gridded fields of 3-h accumulated total precipitation and is based on total precipitation values exceeding 0.01" (0.254 mm) anywhere in a zone during the 3-h period. Experience from the warm season forecast exercises suggests that more than 95% of the total precipitation over Florida is generated by the convective parameterization. The verification of forecast precipitation occurrence is determined using only gridded data from the 0300 UTC initialization of the model since the gridded data from 1500 UTC initialization were not archived as part of the overall meso-eta model evaluation.

The occurrence of observed thunderstorms is determined subjectively from all available 4-km visible (VIS) and IR GOES satellite data and from surface weather reports of rain and thunderstorms. The VIS and IR satellite images at every hour from 1500 to 0000 UTC are animated to locate distinct anvils in the VIS data and strong gradients of cold cloud top temperatures in the IR data. These features are used as a proxy for the occurrence of precipitation in each zone during the 3-h periods. It is likely that anvil debris, cirrus clouds, or the lack of well-defined anvils or cold cloud tops affect the accuracy of this satellite-based, subjective technique in delineating areas of actual precipitation. Therefore, routine surface airway observations of precipitation (i.e. rain or thunderstorms) are included to account for such deficiencies. It is important to point out that surface weather observations alone probably underestimate the occurrence of precipitation given the nonuniform distribution and relative coarse spacing of the stations. In cases where either satellite data or surface observations are missing for the entire 3-h period, the remaining available data are used to identify observed thunderstorms. When both satellite data and surface observations are available, observed thunderstorms are identified in the 3-h window if either data type indicates their presence based on the criteria discussed above.

The occurrences of all forecast and observed thunderstorms as determined from available warm season data in the six zones over each 3-h period are counted and entered in four-cell contingency tables similar to those shown in Table 5.2. In cases where forecast or observed precipitation is located on zone boundaries or across adjacent zones, these events count as "yes" occurrences for each zone containing the specified area of precipitation. The data from these contingency tables are then used to compute the bias, FAR, and POD for each zone and time period. The definitions of the bias, FAR, and POD are given in Table 5.2.

The methodology used in this study for the verification of precipitation occurrence differs from traditional methods. The traditional methods used to verify precipitation involve a point-by-point comparison of forecast and observed amounts at selected thresholds (e.g. 0.01", 0.25", etc.) over the model grid (e.g. Olson et al. 1995). The statistics such as bias, FAR, POD, and threat score or critical success index derived from such analyses do not usually account for spatial errors in forecasting precipitation. On the other hand, these methods often verify forecast and observed precipitation over periods of 12 to 24 h which allows for significant errors in forecasting the temporal evolution of precipitation.

The technique used is this study focuses on the occurrence of precipitation (> 0.01") anywhere within a region on the order of 100 km x 200 km. As illustrated in section 5.2.1.1, the 29-km eta model does not resolve small-scale thunderstorms and associated precipitation. However, experience from the warm season forecast exercises suggests that broad areas of model-generated precipitation could be subjectively correlated with precipitation that was observed over much smaller sections of the same area. By performing a zone assessment of forecast and observed

precipitation occurrence, a far less stringent test of model capabilities is applied than traditional methods which measure exact spatial correlation between forecast and observed precipitation. However, precipitation forecasts in the current evaluation are verified over 3-h periods to highlight temporal errors and determine whether the model can forecast the observed diurnal cycle in warm season precipitation over Florida. In this regard, the evaluation strategy is more stringent than that used in traditional methods especially when precipitation is verified over much longer time periods (e.g. 24 h).

5.2.2.2 Results

Summary statistics for each of the zones are presented in Table 5.6. When all available data are pooled together the sample size of valid forecast/observed data ranges from 73 to 78 depending on zone number and 3-h verification period. Since the sample size is relatively small, it is difficult to determine if subtle differences between the scores in each zone are statistically significant. The following discussion focuses on scores from zone 5 that covers east central Florida and includes XMR (Fig. 5.10).

Within the first 3-h period from 1500 to 1800 UTC, a bias of 1.76 indicates that forecast precipitation occurs 76% more often than actually observed. In later periods, the bias improves to 1.00 between 1800 to 2100 UTC before increasing slightly to 1.21 between 2100 to 0000 UTC. As the bias scores improve, the FAR scores correspondingly decrease. Between 1500 to 1800 UTC, the FAR in zone 5 is 0.52, indicating that the occurrence of precipitation is incorrectly forecast on 52% of valid days. In later periods, the FAR drops to a more respectable 0.30 (1800 to 2100 UTC) and 0.27 (2100 to 0000 UTC). While the bias and FAR show improvement with time, the POD fluctuates without any clear trend. Since values of POD in zone 5 are > 70%, the model tends to accurately forecast the occurrence of most observed rain events. However, these values *must* be viewed in context with values of bias and FAR; a high POD is only effective when the corresponding FAR is low and the bias near unity. Since the contingency table includes observed precipitation regardless of whether it can be resolved by the 29-km eta model, the POD for all zones and time periods may improve (i.e. approach unity) by verifying forecast and observed precipitation only at scales which are resolved by the model.

Table 5.6. Summary statistics for the verification of precipitation occurrence within each of six zones shown in Fig. 5.10. See Table 5.2 for definitions of bias, False Alarm Rate (FAR), Probability of Detection (POD), and Heidke Skill Score (HSS).

Zone 1	15–18 UTC	18–21 UTC	21–00 UTC	Zone 4	15–18 UTC	18–21 UTC	21–00 UTC
Bias	2.44	0.91	0.98	Bias	1.57	0.91	1.28
FAR	0.62	0.20	0.23	FAR	0.52	0.31	0.37
POD	0.94	0.73	0.75	POD	0.76	0.63	0.81
HSS	0.52	0.48	0.66	HSS	0.48	0.53	0.64
Zone 2	15–18 UTC	18–21 UTC	21–00 UTC	Zone 5	15–18 UTC	18–21 UTC	21–00 UTC
Bias	2.05	1.05	1.31	Bias	1.76	1.00	1.22
FAR	0.60	0.24	0.32	FAR	0.52	0.30	0.27
POD	0.81	0.79	0.89	POD	0.84	0.70	0.89
HSS	0.60	0.61	0.78	HSS	0.61	0.58	0.73
Zone 3	15–18 UTC	18–21 UTC	21–00 UTC	Zone 6	15–18 UTC	18–21 UTC	21–00 UTC
Bias	1.74	0.88	1.04	Bias	1.69	0.86	1.00
FAR	0.53	0.19	0.21	FAR	0.53	0.18	0.27
POD	0.81	0.71	0.82	POD	0.79	0.71	0.73
HSS	0.65	0.64	0.78	HSS	0.68	0.66	0.72

Examination of the contingency tables used for the analysis (not shown) reveals that precipitation was observed (forecast) in zone 5 on 32% (57%), 51% (51%), and 58% (70%) of valid days during the periods 1500 to 1800 UTC, 1800 to 2100 UTC, and 2100 to 0000 UTC, respectively. A comparison of these percentages indicates that the bias approaches unity during the last two times periods due to increases in the frequency of observed precipitation. In general, the 0300 UTC initialization of the meso-eta model forecasts precipitation too frequently during the first 3-h period from 1500 to 1800 UTC (1100 to 1400 EDT). However, within the later afternoon and early evening periods from 1800 to 2100 UTC and 2100 to 0000 UTC, the model shows more utility in delineating whether precipitation is likely to be observed in a specific zone. These results are supported by the HSS, which indicates that the model provides the greatest improvement over random forecasts (i.e., HSS = 0) in the later time period. While this discussion only focuses on scores for zone 5, Table 5.6 shows similar results for the other zones.

For the period from 2100 to 0000 UTC, the bias (FAR) of 1.28 (0.37) and 1.22 (0.27) in zones 4 and 5, respectively indicates that the model overestimates the occurrence of precipitation along the central and northeast coast of Florida during the entire warm season. These results are consistent with the example shown in case 2 where model precipitation is forecast from 2100 UTC 9 to 0000 UTC 10 August in zones 4 and 5 but is not supported by surface and IR satellite data. The analysis of precipitation occurrence for the entire warm season is designed to quantify added value to the user by determining how often the meso-eta model produces precipitation forecasts such as those shown for case 1 versus case 2 in section 5.2.1. Such verification is useful since conclusions drawn about model capabilities in forecasting warm season precipitation over Florida are limited by examining only two cases which essentially represent the best and worst of meso-eta model capabilities. Moreover, the verification provides a summary of the times and areas over which the meso-eta model is most capable of generating useful convection forecasts given the wide variety of different scenarios encountered during the warm season.

5.3 Tropical Wave Verification

The capability of the meso-eta model to forecast the development and movement of warm season tropical disturbances was documented as part of the daily forecast exercises. For the purposes of this evaluation, tropical disturbances (or tropical waves; TW) include both easterly waves (Riehl 1954, Carlson and Lee 1978) and tropical upper tropospheric troughs (TUTT; Sadler 1975, Whitfield and Lyons 1992) that typically move from east to west and are easily identified by the motion of an organized and distinct area of enhanced convection. Although Atlantic tropical storm and hurricane activity was above-average during the summer of 1996, there are few TW which entered the subset model domain (e.g. the area shown in Fig. 5.1). In fact, during the warm season forecast exercises only seven potential TW cases were documented which were not tropical storms or hurricanes.

A post-seasonal examination of forecast graphics and satellite imagery reveals that only one of these cases persisted within the subset model domain for longer than 2 subsequent forecast periods. Given only one case example, no conclusions should be drawn regarding how accurately the 29-km eta model forecasts the development and movement of TW. However, experience from the warm season forecast exercises suggests that persistence of wave features such as a cyclonic turning of the lower tropospheric winds or weak sea-level pressure troughs between subsequent model runs for 2 or 3 days is important for classifying potential TW. In particular, the meso-eta model often generates small-scale waves which propagate around the southwestern edge of the large-scale sub-tropical anticyclone. These features have typical wavelengths on the order of 100's of km while the horizontal scale of TW in the lower troposphere is on the order of 1000 km. Although these small-scale waves sometimes help focus developing convection across Florida, they should not be interpreted as TW due to their small size and lack of persistence between subsequent model runs.

5.4 Cold Front Verification

Fronts are usually identified as a line of confluent winds that precede narrow zones of tight gradients in temperature and/or dew point temperature (Wallace and Hobbs 1977). Cold fronts in particular represent the leading edge of a transition zone to a relatively colder, drier air mass. An extensive review of theoretical and observational studies on fronts is provided by Bluestein (1986), Keyser (1986), and Carlson (1991). While mesoscale sea-breeze fronts are common during the warm season in Florida, synoptic-scale cold fronts are frequent during the cool season. These synoptic-scale, cool season cold frontal passages through central Florida are commonly associated with locally adverse weather which may include extensive precipitation, low visibility, strong horizontal and vertical wind shear, and cold temperatures. Moreover, the environment associated with synoptic-scale cold fronts contains instabilities that are conducive for the intensification of mesoscale weather phenomena (Keyser 1986). Given these possibilities, meso-eta forecasts of synoptic-scale cold frontal passages through east-central Florida (hereafter referred to as fronts, or cold fronts) are compared with observations for the cool season period October 1996 through January 1997. A single case example is presented which considers some aspects of the meso-eta model's capabilities and limitations in depicting small-scale details of cold frontal passages. Finally, a summary is provided which compares the observed and forecast timing of frontal passages at XMR throughout the cool season evaluation period.

5.4.1 Case Example

The example presented here is an analysis of a forecast and observed cold frontal passage through central Florida on 8 to 9 November 1996. The meso-eta forecast for this case is from the 0300 UTC cycle on 8 November 1996 with frontal passage at XMR occurring later that day near 2200 UTC. Animation of diagnostic quantities for the meso-eta forecast grids such as vorticity, vertical velocity, convergence, moisture and temperature advection, convective parameters, etc., provide useful ways to depict the forecast evolution of the atmosphere. Unfortunately, the sparsity of observational data limits verification of the forecasts, particularly over offshore areas to the west and east of the Florida peninsula. Use of the KSC/CCAS mesonet data for verification of this case is not appropriate because the width of the transition zone associated with the forecast synoptic-scale cold front is larger than the area covered by the mesonet. For these reasons only general, subjective comparisons between the forecast and observations are made in terms of cloud cover, precipitation, low-level winds and dew point temperatures, and upper air and surface data at XMR.

5.4.1.1 Clouds and Precipitation

On 8 November 1996, a surface cold front associated with a developing cyclone was oriented generally in a northeast to southwest direction and extended through the Carolinas, Georgia, and northern Florida. As the front propagated through central Florida, forecast total cloud fraction and 3-h total precipitation amounts are compared with 4-km IR satellite imagery and observed precipitation composites (Fig. 5.11). Model forecast cloud fraction depicts the percentage of cloudy area in a grid box and is estimated using relative humidity within all model layers (Zhao et al. 1997). Hourly precipitation composites are derived by NCEP using a combination of available Office of Hydrology rain gauge observations and NEXRAD-derived precipitation estimates (Baldwin and Mitchell 1996). The precipitation amounts shown in Fig. 5.11 are derived by summing the hourly NCEP composite amounts over the 3-h forecast period. Note that observed precipitation amounts shown in Fig. 5.11f represent only a 2-h accumulation because the 2200 UTC precipitation estimate is not available.

At 1800 UTC 8 November, the model depicts a northeast to southwest oriented band of clouds approximately 500 km wide moving across the Florida peninsula (Fig. 5.11a). Cloud fractions of

100% are forecast to exist in a narrow band from around Jacksonville (JAX) to Tampa Bay (TBW), FL and southwest into the Gulf of Mexico. In conjunction with this narrow band of 100% cloud cover, 3-h forecast precipitation amounts between 1500 and 1800 UTC exceed 0.75″ from near JAX to TBW. In comparison, 4-km IR imagery (Fig. 5.11b) reveals that observed clouds cover approximately the same area as depicted by the forecast cloud cover. In particular, scattered cloud cover is observed over south Florida and over most areas of the Atlantic where forecast cloud fractions are generally less than 70%. Observed clouds appear more dense in the satellite imagery along the same line where the model predicts 100% cloud fractions. Observed precipitation is heaviest along a line that is slightly northwest of the axis of maximum precipitation forecast by the model at 1800 UTC 8 August

Figure 5.11. Forecast total cloud fraction and 3-h precipitation in panels a-c with corresponding 4-km GOES IR imagery and estimates of observed 3-h precipitation in panels d-f. Charts are shown at 3-h intervals from 1800 UTC 8 November through 0000 UTC 9 November as labeled in each panel. Forecast total cloud fraction is shaded from 0% (darkest) to 100% (lightest) at intervals of 10%. The 3-h forecast and observed precipitation is accumulated from 1500 to 1800 UTC, 1800 to 2100 UTC, and 2100 to 0000 UTC with isopleth intervals at 0.01, 0.10 (dashed), 0.25, 0.50 and 0.75". In panel (f), observed precipitation is accumulated for 2 h due to missing data at 2200 UTC. Station identifiers for Jacksonville, FL (JAX) and Tampa Bay, FL (TBW) are shown in panel (f).

(compare Figs. 5.11a, b). Locally intense 3-h observed accumulations exceed 1.0″ off the west coast of Florida.

At 2100 UTC, the area of forecast and observed clouds and precipitation propagates to the southeast by about 100 km (Figs. 5.11c, d). The heaviest forecast 3-h precipitation amounts across central Florida are again in excess of 0.75″. To the northeast of TBW, observed 3-h accumulations (Fig. 5.11d) are locally in excess of 0.25″. Again, the area covered by precipitation is forecast remarkably well but the model cannot predict the small-scale details. Model cloud fraction forecasts continue to be in agreement with the satellite imagery at 2100 UTC. Cloud fractions of 100% remain collocated with the area where brighter cloud tops are observed across central Florida.

The area of clouds and precipitation associated with this cold front continued to move to the southeast through 0000 UTC 9 November (Figs. 5.11e, f). However, the previously banded structure in the precipitation field becomes more intricate as it breaks apart into smaller sections. While observed 3-h rainfall amounts between 1800 and 2100 UTC locally exceed 0.25″ across central Florida, 2-h accumulations in the same area reach just 0.10″ between 2100 and 0000 UTC. Meanwhile, a new band of heavy precipitation formed offshore over the Atlantic with 2-h rainfall amounts in excess of 1.0″ (Fig. 5.11f). As is consistent with all previous case examples, the meso-eta model is not capable of resolving the small-scale details of these changes in the cold frontal rainband structure. However, the model does predict a general decrease in precipitation amounts across central Florida with a corresponding split in the primary cold frontal rainband (Fig. 5.11e).

Examination of hourly point data for this case indicates that 0.36″ of rainfall was forecast by the model at XMR, mostly between 2000 and 0000 UTC. Surface observations at XMR reveal that a light rain shower at 2104 UTC produced merely 0.06″ of rain. Although the forecast amount of rainfall is excessive at XMR, the forecast grids shown in Fig. 5.11e indicate that amounts could have been much greater if the model did not accurately forecast the decrease in intensity and split in the rain band. The model forecast is able to predict the larger-scale area covered by cloud and precipitation for this case with remarkable accuracy.

5.4.1.2 Winds and Dew Point Temperatures

While the animation of cloud cover and precipitation forecasts are useful for identifying the extent and motion of weather associated with cold frontal passages, surface data are required to track the position of the cold front. The parameters used to identify the position of the frontal zone near the surface usually include winds, pressure (heights), moisture, or temperature. For this particular case example, winds and dew point temperatures provide the strongest representation of frontal position. In Fig. 5.12, forecast 1000-mb dew point temperatures and 10-m wind streamlines are plotted along with available surface observations at 2100 UTC 8 November 1996.

For this example, a line of sharply confluent winds appears in the forecast streamlines to the east of the Florida peninsula (Fig. 5.12). This line precedes the leading edge of rapidly decreasing forecast dew point temperatures across central Florida. A heavy line on the figure corresponds to the location of the cold front inferred by forecast wind direction and dew point temperatures. Observations of wind and dew point temperature plotted on the figure agree reasonably well with the corresponding forecast parameters. In particular, wind directions generally match those indicated by the forecast streamlines although discrepancies exist especially along Florida's southeastern coast. Observed dew point temperatures are within about ±2 ˚C of forecast values and clearly indicate a sharp decrease to the northwest across central Florida. Based on observed dew point temperatures and wind directions, the position of the leading edge of the observed frontal zone also appears to lie close to the forecast frontal position (heavy line in Fig. 5.12).

Examination of wind directions and dew point temperatures indicate that the forecast and observed frontal zones appear to be nearly collocated at 2100 UTC 8 November 1996. However, closer examination of Fig. 5.12 reveals that there are differences in the horizontal scale of the forecast and observed frontal zones. In particular, the forecast wind direction shift appears to be more gradual than observed. Forecast winds shift from southwest just offshore Cape Canaveral to northwest along the west coast of Florida. A similar wind shift is observed in the observations over the much shorter distance between Titusville (TIX) and Orlando International Airport (MCO) in east central Florida. Although the model appears to forecast the location of the frontal zone quite accurately across central Florida, the 29-km grid point resolution is not adequate to capture the sharpness of the observed cold front.

Figure 5.12. Forecast 10-m wind streamlines and 1000-mb dew point temperatures (˚C) with available observations of surface wind (kt) and dew point temperatures (˚C) at 2100 UTC 8 November 1996. Forecast dew point temperatures are shown in gray shading every 2 ˚C with darker shading representing drier air as indicated on the temperature scale. Long (half) barbs represent 10 (5) kt wind observations with numerals shown for dew point temperature observations. Station identifiers are given for MCO and TIX.

5.4.1.3 Point Forecasts at XMR

It is possible to identify the time when the leading edge of the frontal zone passes through XMR using hourly surface data. Before using meteograms of hourly surface data to identify frontal passages at a point, it is necessary to note the existence of the approaching front in the horizontal distribution of forecast and/or observed data. When considered alone, time series of surface parameters sometimes exhibit shifts which could be misinterpreted as frontal passages. For the 8 to 9 November 1996 case, a front has already been identified using precipitation, cloud fraction, and surface wind and dew point temperature (Figs. 5.11, 5.13). The figures and corresponding discussion demonstrate that the forecast and observed cold fronts stretch across central Florida around 2100 UTC and are clearly identifiable by the dew point temperature gradient and wind shift.

Forecast and observed meteograms of temperature, dew point temperature, mean sea-level pressure (MSLP), wind speed, and wind direction at XMR are shown in Fig. 5.13 for the 33-h period from 0300 UTC 8 November through 1200 UTC 9 November 1996. At 2200 UTC, observed dew point temperatures begin to decrease rapidly at the rate of about 5 ˚C hr^{-1} (Fig. 5.13b). Forecast dew point temperatures also begin decreasing at that time, though at a slower rate relative to observations. A sudden shift in observed wind direction (Fig. 5.13e) is also observed at 2200 UTC. The corresponding forecast wind shift is more gradual, yet clearly evident. The meteograms of dew point temperature and wind direction (Figs. 5.13b, e) indicate that the leading edge of the forecast and observed frontal zone passes through XMR around 2200 UTC 9 November 1996. This is not surprising given the forecast and observed position of the front previously noted in Fig. 5.12 using wind shifts and dew point temperature gradients.

Other parameters displayed in the meteograms (Fig. 5.13) do not show as clear a depiction of when the front arrives at XMR. For example, forecast and observed temperatures begin to decrease prior to the frontal passage simply in response to the normal diurnal cooling near sunset. Wind speeds in this example show a steady increase with time, but there is no indication of a sudden jump in wind speed which sometimes accompanies a cold frontal passage. The time of frontal passage at XMR may not be inferred directly from MSLP but increasing values at 2200 UTC lend support to the fact that pressures are rising as a ridge builds in behind the advancing cold front.

It is interesting to note that forecast changes in meteogram parameters occur more slowly than observed. For example, at 2200 UTC, the observed winds at XMR shift from about 210 to 300˚ in one hour. The same shift in forecast wind direction occurs gradually over four hours from about 2000 UTC 8 to 0000 UTC 9 November. As discussed in section 5.4.1.2, similar changes in wind direction also occur over a shorter horizontal distance in the surface observations than in the forecast streamlines. Therefore, hourly meteogram data also indicate that the meso-eta model does not resolve the sharp gradients of temperature, moisture, wind, etc. at the scales which are characteristic of observed frontal zones.

The passage of the cold front through XMR is also apparent in forecast and observed profiles of upper air temperature, dew point temperature, and winds. The forecast and observed soundings at XMR 10-h prior, 2-h after, and 14-h after frontal passage are depicted in Figs. 5.14a, b, and c, respectively. The soundings reveal that the model generally is able to handle the increase in moisture as clouds and precipitation enter central Florida and the subsequent drying that occurs after frontal passage. Moreover, the depth of the post-frontal intrusion of cold air is evident by the low-level temperature inversion and wind shifts that develop in the lower 200 mb of both forecast and observed soundings (Fig. 5.14c).

Figure 5.13. Forecast and observed meteograms at XMR of 2-m temperature (panel a) , 2-m dew point temperature (panel b), mean sea-level pressure (MSLP; panel c), 10-m wind speed (panel d) and 10-m wind direction (panel e). The meteograms cover the 33-h period from 0300 UTC 8 November through 1200 UTC 9 November 1996. Solid lines depict forecast values from the 0300 UTC meso-eta model run, dotted lines depict observed values, and the vertical dashed lines indicate the apparent time of frontal passage through XMR at 2200 UTC 8 November. The horizontal dashed line in panel e is added for emphasis.

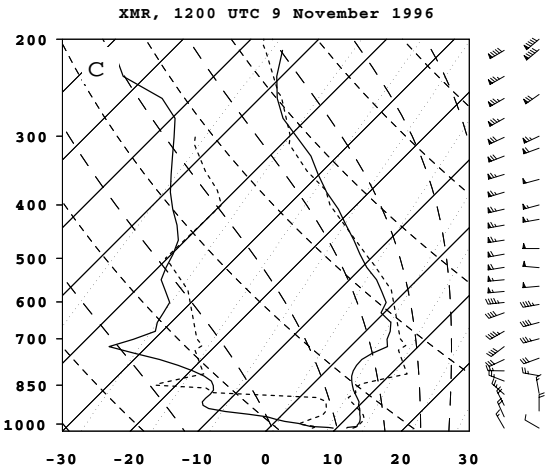

Figure 5.14. Skew-t plots of forecast and observed sounding data at XMR valid (a) 1200 UTC 8 November 1996, (b) 0000 UTC 9 November, and (c) 1200 UTC 9 November. All forecasts are taken from the model run initialized 0300 UTC 8 November 1996. Heavy solid (dashed) lines are forecast (observed) temperature and dew point temperatures (˚C). Forecast (observed) wind barbs (kt) are shown in bold (normal) to the right of each skew-t plot.

Many of the differences between the forecast and observed variables shown in Figs. 5.13 and 5.14 are consistent with the cool season objective verification of those parameters. For example, dew point temperatures and wind speeds following cold frontal passage are greater than observed (Fig. 5.13b, d). A similar positive bias appears in the statistics shown in Figs. 4.2b and 4.4b. The forecast temperature inversion that develops near 700 mb after frontal passage (Fig. 5.14c) is at a higher level than observed. This result is consistent with the cool season biases shown in Fig. 4.15a which depict a sharp cool bias at around the same level. In spite of these few notable difficulties, the meso-eta forecasts of most parameters for this case of frontal passage are reasonably accurate. Again, this result is consistent with the fact that biases for most parameters discussed in section 4 are relatively small.

5.4.2 Cold Frontal Timing at XMR

The case example discussed in section 5.4.1 demonstrates some of the capabilities and limitations of the meso-eta model in forecasting cold frontal passages through central Florida. However, not all forecasts of frontal passages are quite as accurate. Many cases are much more complicated and involve phenomena such as pre-frontal rain bands, developing cyclogenesis, and stalled fronts. In an attempt to quantify the overall accuracy of cold front forecasts in central Florida, the timing of cold frontal passages through XMR is documented throughout the cool season period.

In order to perform a verification of frontal passages at XMR, all available 0300 UTC forecast grids are examined for the presence of fronts. As discussed earlier, it is difficult to identify frontal passages using meteograms alone without prior knowledge that a front exists in the domain. Therefore, 0300 UTC meso-eta forecasts of MSLP, 10-m winds, 850-mb vertical velocity, 2-m dew point temperature, and 1000-mb frontogenesis are all used to help identify the movement of cold fronts across central Florida. Frontogenesis is easily derived from forecast winds and potential temperature using GEMPAK and is used to quantify the rate of increase of the magnitude of the temperature gradient with time (Carlson 1991, p. 351). Once the frontal passage events are identified, forecast and observed meteograms are studied over the corresponding periods to determine the time of frontal passage to the nearest hour.

On each of the days in which a frontal passage is evident in the forecast grids, hourly point forecast and observed surface data at XMR are plotted as meteograms similar to those shown in Fig. 5.13. Although all five variables are considered simultaneously, shifts in wind direction to the west or northwest and rapid decreases in dew point temperatures are primarily used to identify the frontal passage at XMR. Shifts in temperatures, MSLP, and wind speed are occasionally useful to help support the identification of frontal passage based on dew point temperature and wind. Results of forecast and observed frontal passages through XMR are summarized in Table 5.7.

A total of ten observed fronts pass through XMR during the cool season period on days for which both gridded and point forecast data and observed surface data at XMR are available. Several other cold fronts entered northern Florida, however, they are not counted in this summary because observations indicate that the fronts never actually reach XMR. Of the cases considered in Table 5.7, more than half of the forecast cold fronts passed through XMR within one hour of the observed frontal passage. For the 0900 UTC 19 December event, the cold front is not evident at the end of the 33-h forecast cycle beginning 0300 UTC 18 December, as indicated by the word "None" in Table 5.7. Overall, timing accuracy does not appear to depend on forecast duration. Model runs initiated at 0300 UTC are slightly more accurate in forecasting cold frontal passage at XMR than those initiated at 1500 UTC. However, this result may be due to the small number of cases sampled during this cool season period.

The timing and motion of cold fronts through XMR has been documented for the cool season evaluation period. In addition, a limited case study has been performed for one front which passed through XMR at 2200 UTC 8 November 1996 in both the forecast and observations. Cool season results reveal that on many days the model is capable of forecasting frontal passages at XMR to the nearest hour. The case example demonstrates that many smaller details of the frontal passage are simulated reasonably well, including the area covered by clouds and precipitation, and the location of the frontal zone in surface parameters. Animation of meso-eta model output may provide users with substantial added value in terms of forecasting the timing, movement, and intensity of weather moving through central Florida in association with cold frontal passages. However, it is important to note that the 29-km resolution of the eta model is not sufficient to resolve the sharpness of observed gradients in temperature, wind, and moisture associated with cold frontal zones.

Table 5.7. Time of forecast and observed frontal passages (FROPA) through XMR for the 1996-1997 cool season evaluation period. Forecast duration indicates the length of the forecast in hours when the forecast front passes through XMR. Timing errors are calculated in hours as observed passage minus forecast passage. In this manner, negative (positive) timing errors indicate that forecast fronts arrived at XMR too late (early). For some days, frontal passages are listed multiple times because the same front is apparent in subsequent model runs.

Observed FROPA at XMR		0300 UTC Forecast Cycle FROPA at XMR				1500 UTC Forecast Cycle FROPA at XMR			
Date	Time (UTC)	Date	Time (UTC)	Duration (hours)	Error (hours)	Date	Time (UTC)	Duration (hours)	Error (hours)
19 Oct	0500	19 Oct	0900	30	-4	Not available			
		19 Oct	0600	3	-1				
3 Nov	0200	2 Nov	2300	20	+3	3 Nov	0300	12	-1
8 Nov	2200	8 Nov	2200	19	0	8 Nov	2200	31	0
						8 Nov	2300	8	-1
22 Nov	1200	22 Nov	1300	10	-1	22 Nov	1400	24	-2
26 Nov	1700	26 Nov	1700	14	0	26 Nov	1900	4	-2
2 Dec	0900	2 Dec	0900	30	0	2 Dec	1200	21	-3
		2 Dec	0900	6	0				
8 Dec	1000	8 Dec	0900	6	1	8 Dec	1200	21	-2
19 Dec	0900	None		30		19 Dec	1300	22	-4
		19 Dec	1000	7	-1				
9 Jan	2300	10 Jan	0200	23	-3	10 Jan	0400	13	-5
16 Jan	1700	16 Jan	1900	16	-2	16 Jan	1800	27	-1
						16 Jan	2300	8	-6

5.5 Verification of Warm and Cool Season Winds

The original evaluation protocol called for the subjective verification of warm season steady-state winds exceeding 18 kt and selected warm or cool season case studies of mesoscale wind features identified from time-height sections of 50-MHz and/or 915-MHz profiler data. During the 1996 warm season, the standard, hourly airways observations at XMR indicate winds ≥ 18 kt on six days primarily in response to nearby thunderstorms. The 0300 UTC meso-eta model runs archived during the warm season did not forecast winds ≥ 18 kt at XMR. Furthermore, the point forecasts from the 1500 UTC model runs indicate winds ≥ 18 kt on only two occasions, neither of which correlate with observed convective events. In general, the meso-eta model forecasted wind ≥ 18 kt during either season only in the presence of strong pressure gradients associated with tropical and/or extratropical cyclones, fronts, etc. For this reason, no additional verification is performed to assess the utility of the meso-eta model in forecasting convective winds ≥ 18 kt during the warm season.

The evaluation protocol specifies that hourly time-height wind forecasts at XMR were to be verified using 50-MHz and 915-MHz profiler data and wind observations from the KSC/CCAS tower network. However, the 915-MHz profiler data were not routinely archived until after the end of cool season evaluation period. Although 50-MHz profiler data were archived, no analysis of wind events is possible below the lowest gate of the profiler at roughly 2 km. On the other hand, the KSC/CCAS towers sample only the lowest levels of the atmospheric boundary layer near the surface. Finally, model users indicated during the pre-final report discussions that results obtained from one or two cases would be too limited unless they could be generalized for the entire season as done for

the sea-breeze and thunderstorm verification. Based on these problems with data and potential limitations with the analyses, case studies of mesoscale wind features were not performed.

5.6 Verification of Cool Season Cloud Forecasts

The selection of cool season cloud cases was based on more challenging forecasts such as the development of stratocumulus clouds that occurs frequently in the cool season following the passage of a cold front. The evaluation was designed to determine if the 29-km eta model provides any added value for such forecasts verified using surface and launch reconnaissance aircraft observations and XMR rawinsonde relative humidity profiles. As with the wind analysis, there was concern expressed during the pre-final report discussions that limited verification of explicit cloud water and/or relative humidity forecasts from one or two cases is not sufficient to reveal overall model capabilities in forecasting clouds. Since a more detailed and complete verification of meso-eta model cloud forecasts over the warm and/or cool season is beyond the scope of the current evaluation, no cases studies of cloud forecasts were performed.

6.0 Summary and Lessons Learned

This section summarizes results from the objective verification of meso-eta model point forecasts and the subjective verification of sea breezes, thunderstorms, and cold fronts. The section concludes with a general summary and lessons learned from the overall meso-eta model evaluation.

6.1 Summary of Objective Verification

The objective verification of the eta model focused on the overall accuracy of wind, temperature, and moisture forecasts at XMR, TBW, and EDW for the warm and cool seasons. The statistical measures used to quantify model forecast errors are the bias, RMS error, standard deviation, and consistency. Using these statistics, point forecasts from the 0300 UTC and 1500 UTC meso-eta model cycles are verified against standard surface and rawinsonde observations. Convective parameters and 850 to 500-mb layer-averaged wind and relative humidity are derived from the forecast soundings and verified against corresponding values from observed soundings. As specified in the evaluation protocol, results were stratified by the 950- to 600-mb layer-averaged wind direction. However, examination of results for every parameter indicates that error characteristics are qualitatively similar under both westerly and easterly flow regimes. For this reason, all available data are combined and final results are not stratified by wind regime.

6.1.1 Surface Parameters

Overall, results of the surface parameter verification reveal that forecast errors are on average reasonably small. However, there are a few identifiable biases which include overestimation of dew point temperature and wind speed during the cool season at XMR and diurnal changes in warm season temperature, wind speed, and MSLP at EDW.

The only benchmark specified in the evaluation protocol is a comparison of 10-m winds with 1 to 6-h persistence. Results of this benchmark reveal that 1- to 3-h persistence forecasts of wind speed and direction usually have smaller RMS errors than the corresponding meso-eta model forecasts. However, the model forecasts of these variables are occasionally more accurate than 6-h persistence.

In general, RMS error trends for most parameters reveal that the model exhibits minimal error growth throughout the 33-h forecast period. The error variance often comprises a large portion of the total error. This suggests that errors in surface parameters are commonly due to more random, non-systematic variations in the forecasts and/or observations. Consistency results indicate that subsequent model runs tend to agree more closely with one another than with observations. Since the magnitude of errors depends on parameter, location, and season, it is difficult to specify whether the model is generally more accurate in forecasting surface parameters during the warm or cool season.

6.1.2 Upper Air Parameters

Examination of results for all upper air parameters reveals that errors are qualitatively similar for both the 0300 and 1500 UTC forecast cycles. Therefore, sounding data from both model cycles are combined while performing the verification of upper air parameters. As with surface variables, forecast errors for upper air parameters are on average reasonably small. RMS error trends among each of the three available verification periods indicate that the model exhibits minimal error growth. Consistency results again suggest that subsequent model runs tend to agree more closely with one another than with observations.

For many parameters, a large portion of error standard deviations may be explained, in part, by rawinsonde measurement uncertainty. As with surface forecasts, error variances provide large contributions to the total error. There are a few identifiable biases which include difficulties in resolving tropopause heights and cool season lower tropospheric temperature inversion heights at XMR and TBW. In addition, warm (cool) season forecast errors at XMR and TBW indicate a cool, dry (warm , moist) bias which suggests that forecast soundings are on average more (less) stable than observed.

6.1.3 Convective Indices and 850 to 500-mb Layer-Averages

During the warm season, negative biases in precipitable water (PWAT) and convective available potential energy (CAPE) and positive biases in the lifted index (LIFT) indicate that forecast soundings are typically drier and more stable than observed. These errors are consistent with lower tropospheric warm season biases in mixing ratio and temperature at XMR which indicate that forecasts tend to be thermodynamically more stable than observed. During the cool season, positive biases in CAPE and the K index (KINX) and negative biases in LIFT indicate that cool season forecasts are more unstable than observed. These results are also consistent with the low-level warm bias in temperature and moist bias in mixing ratio found during the cool season at XMR. In general, the results of both convective parameter and 850 to 500-mb layer-average verifications are consistent with characteristic biases identified in the upper air statistics.

Errors in forecast convective parameters on any given day may actually be large enough to provide misleading information regarding the likelihood for thunderstorm development. In particular, errors in any given convective index result from errors in moisture, temperature or wind variables which are used to compute the index and may be cumulative (in the vertical), especially for integrated quantities such as CAPE. Therefore, it is important to understand the accuracy and relationships of all variables which are used to derive each index.

6.2 Summary of Subjective Verification

The subjective verification of sea breezes, thunderstorms, and cold fronts is designed to assess the added value of the meso-eta model in forecasting selected aspects of these phenomena. The evaluation strategy consists of limited cases and seasonal verification. Seasonal verification quantifies the added value and is important because conclusions drawn about model limitations and capabilities in forecasting the aforementioned phenomena are limited by examining only a few cases.

6.2.1 Sea Breezes

The analysis of the forecast and observed sea-breeze development from 7 June 1996 demonstrates that the meso-eta model forecasts a sea breeze that is characterized by a peninsula-scale thermally direct circulation. The thermally direct circulation is driven by differential heating across the land/sea boundaries along the Florida peninsula. The features associated with the forecast sea breeze identified from 3-h model output include a thermal trough in sea-level pressure over the peninsula, shift in 10-m level wind direction from offshore to onshore flow, and low-level convergence and vertical motion patterns oriented parallel to the coastlines. Based on the results from this single case, the meso-eta model appears to depict an evolution of the sea breeze that is dynamically realistic although at a larger scale than observed. It is important to note that the 29-km horizontal resolution of the model is not sufficient to resolve the individual circulations associated with east or west coast sea breezes. Instead, the model generates a single low-level convergence zone and an associated circulation that generally lies parallel to the coastlines.

The sea-breeze verification is also designed to determine how reliably the meso-eta model forecasts the occurrence of east or west coast sea breezes anywhere along the Florida peninsula during the entire warm season. This portion of the analysis is important because previous studies have shown that the timing and location of convection over Florida is modulated by interactions between the sea-breeze circulations and synoptic-scale flow. The results indicate that the 0300 UTC model runs correctly forecast the occurrence of sea breezes about 50% of the time they are observed during the warm season. The utility of sea-breeze forecasts may be limited for this reason and the fact that the meso-eta model resolves only the larger-scale aspects of the observed sea breeze. In some cases, the failure of the model to forecast the occurrence of the sea breeze is likely due to larger-scale forecast errors over a significant portion of Florida.

6.2.2 Thunderstorms

Two cases are presented of forecast and observed thunderstorm development on 1 to 2 August 1996 (case 1) and 9 to 10 August 1996 (case 2). The first example shows a best-case scenario when the meso-eta model depicts a remarkably accurate forecast of developing convection in the late-afternoon and early evening across the Florida peninsula. The second case illustrates an alternative scenario when the model forecasts excessive precipitation along much of Florida's east coast during the same time period. The results from these and other warm season cases (not shown) suggest that the model generates broader areas of organized convection which, on occasion, are remarkably accurate. In contrast, there are a number of instances during the warm season when the model did not forecast areas of organized convection or the evolution of individual thunderstorms that produced significant weather. This result is expected because the 29-km horizontal resolution of the meso-eta model is too coarse to resolve convection at those scales.

Since a wide variety of scenarios for the development of forecast and observed convection were observed during warm season forecast exercises, a verification of precipitation occurrence is required in order to quantify the utility of the model in forecasting warm season convection. Given the limitations in resolving small-scale convection, traditional precipitation verification using point-to-point comparison at selected thresholds was not done. Instead, verification of precipitation over 3-h periods in zones on the order of 100 km x 200 km is performed for all available warm season days. The technique does not specifically address precipitation verification within 25 miles of XMR as specified in the original evaluation protocol. However, it does provide a means to quantify the accuracy of the model in forecasting the occurrence of larger areas of organized convection without requiring that the model produce the correct amount of precipitation at exactly the location where it is observed.

The bias in all zones over Florida from 1500 to 1800 UTC ranges from 1.69 to 2.44 indicating that the meso-eta model forecasts precipitation to occur more often than observed. During later time periods from 1800 to 2100 UTC and 2100 to 0000 UTC, the bias, POD, and FAR in all zones indicate that the meso-eta model shows more utility than in the earlier period (1500 to 1800 UTC) in successfully delineating whether precipitation will occur in a specific zone. The statistical scores such as bias for zone 5 improve with time in part due to an increase in frequency of observed precipitation within that zone. Since observed precipitation is counted in the contingency tables regardless of scale, the statistics may improve further by excluding observed precipitation events such as isolated thunderstorms which can not be resolved by the model.

The verification of warm season precipitation occurrence indicates that the model generates excessive precipitation from 1500 to 1800 UTC despite the fact that biases in convective parameters such as CAPE and LIFT show that 1000 UTC forecast soundings are on average typically drier and more stable than observed. At least 95% of the warm season forecast precipitation over Florida is

produced by the convective scheme in the meso-eta model. It is possible that forecast soundings destabilize too rapidly after 1000 UTC thereby triggering the convective parameterization which eventually produces precipitation more often than it is actually observed. For example, the erroneous precipitation forecast in case 2 may be related to excessive moisture convergence and instability as documented by a comparison of forecast and observed soundings at XMR along the east coast. However, more comprehensive analyses of model output and additional observations are required to diagnose the reasons for both accurate and inaccurate forecasts of convective precipitation throughout the warm season.

6.2.3 Cold Fronts

The analysis of a cold front which passed through central Florida on 8 to 9 November 1996 demonstrates some of the meso-eta model's capabilities and limitations in depicting the timing and motion of cold frontal passages. The case reveals that although the model is not able to predict the small-scale details, it is capable of forecasting the larger-scale areas covered by clouds and precipitation with remarkable accuracy. Moreover, the location of the leading edge of the frontal zone near the surface is in agreement with observations of winds and dew point temperatures. Although the model appears to forecast the location of the frontal zone quite accurately across central Florida, the 29-km grid point resolution is not adequate to capture the sharpness of the observed cold front.

Hourly plots of 2-m dew point temperature and 10-m wind direction for this case reveal that the leading edge of both forecast and observed frontal zones pass through XMR within the same hour. It is interesting to note that shifts in forecasts of surface parameters are more gradual than corresponding shifts in observed data as the front passes XMR. This result supports the idea that the meso-eta model does not resolve the sharp gradients of surface temperature, moisture, wind, etc. at the scales which are characteristic of observed frontal zones. Forecasts of most parameters for this case of frontal passage are generally quite accurate, a result which is consistent with the relatively small biases noted earlier for the entire cool season. In fact, a verification of cold front timing at XMR over the entire cool season reveals that the model is accurate to within the nearest hour for a majority of documented cold frontal events.

6.3 Overall Evaluation Summary and Lessons Learned

The evaluation described in this report is designed to assess the utility of the meso-eta model for local weather forecasting in support of 45WS, SMG, and NWS MLB operational requirements. In conclusion, the following points summarize overall results from the AMU's year-long evaluation.

- In general, objective verification results reveal that meso-eta model point forecasts at XMR, TBW, and EDW are reasonably unbiased. This result suggests that the model has few substantial systematic errors and on average, can be used reliably. However, there are some exceptions identified in this evaluation as indicated by the following list of model biases.

  2-m dew point temperatures and 10-m wind speeds are typically overestimated at XMR during the cool season.

  Diurnal changes exist in the average forecast errors for 2-m temperature, 10-m wind speed and MSLP at EDW.

  At XMR and TBW, warm (cool) season forecast soundings are typically drier and more stable (unstable) than observed.

The height of the lower tropospheric inversion at XMR and TBW is misrepresented during the cool season.

Tropopause heights are misrepresented by the model at all three stations.

- Objective verification results also indicate minimal error growth with time based on RMS errors. This means that, on average, forecast accuracy does not vary substantially throughout the 33-h forecast period.

- The error variance for many variables comprises a large portion of the total RMS error. In these instances, total model error over the course of an entire season is dominated by the day-to-day variability in forecasts and/or observations.

Subjective verification of sea breezes, thunderstorms, and cold fronts is very important to quantify added value of the model forecasts for these specific phenomena which can not be readily inferred from statistics over many cases (i.e. from objective verification). Moreover, subjective and objective verification are complimentary and results from each component of the evaluation are generally consistent. Some results from the subjective evaluation which can be important for operational forecast concerns include the following.

- The forecast sea breeze is characterized by a peninsula-scale, thermally direct circulation that forms in response to differential heating across the land/sea boundaries along the Florida peninsula. The occurrence of sea breezes are correctly forecast about 50% of the time they are observed during the warm season. The 29-km grid point resolution of the model is not sufficient to resolve the individual circulations associated with the observed west and/or east coast sea breezes.

- Two case studies demonstrate different situations where the model generates both accurate and inaccurate forecasts of larger scale, organized convection. However, the model's 29-km grid point resolution is not sufficient to accurately forecast the development of isolated thunderstorms.

- Cold frontal passages through XMR are often forecast to within the nearest hour of observed passages. The spatial and temporal evolution of weather associated with frontal passages is also depicted well by animation of the 3-h forecast gridded products. However, the ability of the model to represent small scale details such as the width of the surface frontal zone is limited by the model's 29-km resolution.

- Results from the objective verification do not indicate whether the model is more accurate overall during either the warm or cool season. However, results from the subjective verification suggest that the model forecasts over central Florida may be more useful during the cool season. This statement is based on the fact that the meso-eta model resolution is not yet sufficient to resolve the small-scale details of sea and river/lake breeze circulations, thunderstorm outflow boundaries, and other phenomena which play a dominant role in determining the short-term evolution of weather over east central Florida during the warm season.

- Objective verification results also demonstrate that forecasts of selected parameters are reliable over the course of an entire season. On the other hand, results from the subjective verification demonstrate that model forecasts of developing weather events such as thunderstorms, sea breezes, cold fronts, etc. are not always as accurate as implied by the seasonal error statistics.

The AMU's daily real-time warm season forecast exercise proved to be a valuable component of the overall subjective verification because it revealed how operational forecasters could use the 0300 UTC cycle of the meso-eta model for local forecasting. Lessons learned from these daily weather discussions are as follows.

- Animation of 3-h model output with color enhancements and overlay of multiple fields (winds, temperature, etc.) is useful to identify features and trends that could become important for developing weather (as illustrated with sea breeze, thunderstorm, and cold front case examples).

- Availability of digital gridded model output at 3-h intervals is important because it gives users the flexibility to select variables, cross sections, overlay options, contour intervals etc. and it provides the temporal resolution needed to track specific aspects of forecast weather events such as the timing of cold frontal passage, onset of sea breeze, etc.

- The model often generates small scale vortices that are difficult to confirm with observations. Many times, these vortices are not realistic and lead to fluctuations in point forecast variables such as wind direction/speed and convective parameters (as demonstrated in the large error standard deviations of these variables).

- In order to exploit the four-dimensional capability of the meso-eta and other models in forecasting possible realizations of the atmosphere, sufficient communication bandwidth and computer processing power are necessary to retrieve, process, and examine output data. This requirement will become more important in the future as NCEP increases the number of meso-eta model runs per day, the model resolution, and potentially the frequency of model output.

7.0 Future AMU Efforts on 29-km Eta Model Evaluation

The evaluation methodology used for this study is comprised of both objective and subjective components stratified over two 4-month evaluation periods. While this strategy enables an assessment of both forecast accuracy and utility for model users, it also imposes some limitations on the completeness of the verification. In particular, limited samples sizes make it difficult to perform various event- and regime-based stratifications and to apply statistical significance tests to the data. Moreover, results could be affected by interannual variability which can not be determined from a single one-year analysis.

Subjective verifications in this evaluation are limited to simple case studies in order to examine a greater number of phenomenological features which impact 45WS, SMG, and NWS MLB operations. The case studies highlight some of the capabilities and limitations of the meso-eta model but are not designed to fully explore the cause(s) of model errors. Seasonal evaluations of sea breezes, thunderstorms, and cold front timing are designed to quantify how consistently the model provides utility in forecasts of these phenomena. However, more detailed examination of model capabilities and limitations is beyond the scope of the present evaluation given available AMU resources.

As part of ongoing efforts to improve the accuracy and utility of forecast products, NCEP is continuing to update the configuration, initialization, and physical parameterizations of the meso-eta model. These updates could modify some of the seasonal error characteristics identified by the AMU's objective verification of surface and upper air forecasts at XMR, TBW, and EDW. In order to increase the sample size and track possible changes in model accuracy, the objective component of the meso-eta evaluation is being extended to include a second warm and cool season period from May through August 1997 and October 1997 through January 1998, respectively. An extension of the subjective component of the evaluation would also be useful and has been discussed as part of the AMU's annual tasking process. However, it was determined that such an evaluation can not be continued effectively within the scope of the AMU's available resources.

As part of the ongoing meso-eta model evaluation, comparisons will be made for the objective verification results between the two warm season and the two cool season evaluation periods at XMR, TBW, and EDW. A comparison between results from the 1996 and 1997 seasons will highlight any changes in the error characteristics at these stations which may occur in response to updates in the meso-eta model configuration. This analysis is also useful for model users since the 1997/1998 results will be more representative of the meso-eta model's current capabilities.

8.0 References

Ahnert, P. R., 1991: Precision and compatibility of National Weather Service upper air measurements. Preprints, *Seventh Symp. on Meteorological Observations and Instrumentation*, New Orleans, LA, Amer. Meteor. Soc., 221-226.

Atkinson, B. W., 1981: Sea/land breeze circulation. *Mesoscale Atmospheric Circulations*. Queen Mary College. University of London. 125-214.

Baldwin, M., and K. E. Mitchell, 1996: The NCEP hourly multi-sensor U. S. precipitation analysis. Preprints, *11th Conference on Numerical Weather Prediction*, Norfolk, VA, Amer. Meteor. Soc., J95-J96.

Barnes, S. L., 1964: A technique for maximizing details in numerical weather map analysis. *J. Appl. Meteor.*, **3**, 396-409.

Betts, A. K., and M. J. Miller, 1986: A new convective adjustment scheme. Part I: Observational and theoretical basis. *Quart. J. Roy. Meteor. Soc.*, **112**, 677-691.

Black, T. L., 1994: The new NMC mesoscale eta model: description and forecast examples. *Wea. Forecasting*, **9**, 265-278.

Blanchard, D. O., and R. E. Lopez, 1985: Spatial patterns of convection in south Florida. *Mon. Wea. Rev.*, **113**, 1282-1299.

Bluestein, H. B., 1986: Fronts and jet streaks: A theoretical perspective. *Mesoscale Meteorology and Forecasting*, Peter Ray, Editor, Amer. Meteor. Soc., Boston, 216-258.

Boybeyi, Z., and S. Raman, 1992: A three-dimensional numerical sensitivity study of convection over the Florida peninsula. *Bound.-Layer Meteor.*, **60**, 325-359.

Carlson, T. N., 1991: *Mid-Latitude Weather Systems*. Harper Collins Academic, London, 507 pp.

Carlson, T. N., and J. D. Lee, 1978: *Tropical Meteorology*. Pennsylvania State University, University Park, PA, 387 pp.

Davies-Jones, R., D. Burgess, and M. Foster, 1990: Test of helicity as a tornado forecast parameter. Preprints, *16th Conference on Severe Local Storms, Kananaskis Park, Alberta, Canada, Amer. Meteor. Soc.*, 588-592.

desJardins, M. L., S. Jacobs, D. Plummer, and S. Schotz, 1997: N-AWIPS: AWIPS at the National Centers for Environmental Prediction. Preprints, *13th International Conference on Interactive Information and Processing Systems*, Long Beach, CA, Amer. Meteor. Soc., 296-298.

Doswell, C. A, R. Davies-Jones, and D. Keller, 1990: On summary measures of skill in rare event forecasting based on contingency tables. *Wea. Forecasting*, **5**, 576-585.

Evans, R. J., 1996: *Final Report on the Evaluation of the Emergency Response Dose Assessment System (ERDAS).* NASA Contractor Report CR-201353, Kennedy Space Center, FL, 184 pp.

Hoehne, W. E., 1980: *Precision of National Weather Service Upper Air Measurements.* NOAA Tech. Memo. NWS T&ED-16.

Holle, R. L., A. I. Watson, R. E. Lopez, K. W. Howard, R. Ortiz, and L. Li, 1992: *Meteorological studies to improve short-range forecasting of lightning/thunderstorms within the Kennedy Space Center area*. Final Report for Memorandum of Agreement between the Office of Space Flight, NASA and the National Severe Storms Laboratory, NOAA, Boulder, CO, 91 pp.

Janjic, A. I., 1994: The step-mountain Eta coordinate model: Further developments of the convection, viscous sublayer, and turbulence closure schemes. *Mon. Wea. Rev*., **122**, 927-945.

Kalnay, E., G. DiMego, S. Lord, H-L. Pan, M. Iredell, M. Ji, D. B. Rao, and R. Reynolds, 1996: Recent advances in modeling at the National Centers for Environmental Prediction. Preprints, *11th Conference on Numerical Weather Prediction*, Norfolk, VA, Amer. Meteor. Soc., J3-J8.

Keyser, D., 1986: Atmospheric fronts: An observational perspective. *Mesoscale Meteorology and Forecasting*, Peter Ray, Editor, Amer. Meteor. Soc., Boston, 216-258.

Laird, N. F., D. A. Kristovich, R. M. Rauber, H. T. Ochs III, and L. J. Miller, 1995: The Cape Canaveral sea and river breezes: Kinematic structure and convective initiation. *Mon. Wea. Rev*., **123**, 2942-2956.

Leslie, L. M., G. D. Hess, and E. E. Hebjan, 1994: The performance of four global models over the Australian region. *Wea. Forecasting*, **9**, 229-240.

Lilly, D. K. 1986: The structure, energetics and propagation of rotating convective storms. Part II: Helicity and storm stabilization. *J. Atmos. Sci*., **43**, 126-140.

Manobianco, J., 1996: *Report on the Installation and Evaluation of the Mesoscale Atmospheric Simulation System*. NASA Contractor Report CR-201151, Kennedy Space Center, FL, 45 pp.

Mesinger, F., 1996: Improvements in quantitative precipitation forecasts with the eta regional model at the National Centers for Environmental Prediction: The 48-km upgrade. *Bull. Amer. Meteor. Soc*., **11**, 2637-2649.

Mesinger, F., and T. Black, 1992: On the impact of forecast accuracy of the step-mountain (eta) versus sigma coordinate. *Meteor. Atmos. Phys*., **50**, 47-60.

Murphy, A. H., 1988: Skill scores based on the mean square error and their relationships to the correlation coefficient. *Mon. Wea. Rev*., **116**, 2417-2424.

Olson, D. A., N. W. Junker and B. Korty, 1995: Evaluation of 33 years of quantitative precipitation forecasting at NMC. *Wea. Forecasting*, **10**, 498-511.

Panofsky, H. A., and G. W. Brier, 1958*: Some Applications of Statistics to Meteorology*. Pennsylvania State University, University Park, 224 pp.

Pielke, R., 1974: A three-dimensional numerical model of the sea breeze over south Florida. *Mon. Wea. Rev*., **102**, 115-139.

Pielke, R. A., and M. Segal, 1986: Mesoscale circulations forced by differential terrain heating. *Mesoscale Meteorology and Forecasting,* Peter Ray, Editor, Amer. Meteor. Soc., 516-548.

Powell, M. D., S. H. Houston, and T. A. Reinhold, 1996: Hurricane Andrew's landfall in south Florida. Part I: Standardizing measurements for documentation of surface wind fields. *Wea. Forecasting*, **11**, 304-328.

Riehl, H., 1954: *Tropical Meteorology*. McGraw-Hill, New York, 392 pp.

Rogers, E., D. G. Deaven, and G. J. DiMego, 1995: The regional analysis system for the operational "early" eta model: Original 80-km configuration and recent changes. *Wea. Forecasting*, **10**, 810-825.

Rogers, E., T. L. Black, D. G. Deaven, and G. J. DiMego, 1996: Changes to the operational "early" eta analysis/forecast system at the National Centers for Environmental Prediction. *Wea. Forecasting*, **11**, 391-413.

Sadler, J. C., 1975: *The Upper Tropospheric Circulation Over the Global Tropics*. Dept. Meteorology, University of Hawaii, UHMET-75-05.

Schaefer, J. T., 1990: The critical success index as an indicator of warning skill. *Wea. Forecasting*, **5**, 570-575.

Taylor, G. E, M. K. Atchison, and C. R. Parks, 1990: *The Kennedy Space Center Atmospheric Boundary Layer Experiment KABLE Phase II Final Report*, Kennedy Space Center, FL, 366 pp.

Wallace, J. M., and P. V. Hobbs, 1977: *Atmospheric Science - An Introductory Survey*. Academic Press, Inc., San Diego, 467 pp.

Weckwerth, T. M., J. W. Wilson, R. M. Wakimoto, and A. Crook, 1997: Horizontal convective rolls: determining the environmental conditions supporting their existence and characteristics. *Mon. Wea. Rev.*, **125**, 505-526.

Wheeler, M. M., and W. P. Roeder, 1996: Forecasting wet microburst on the Central Florida Atlantic coast in support of the United States Space Program. Preprints, *18th Conference on Severe Local Storms*, San Francisco, CA, Amer. Meteor. Soc., 654-658.

Whitfield, M. B. and S. W. Lyons, 1992: An upper-tropospheric low over Texas during summer. *Wea. Forecasting*, **7**, 89-106.

Zhao, Q., T. L. Black, and M. E. Baldwin, 1997: Implementation of the cloud prediction scheme in the eta model at NCEP. Submitted to *Wea. Forecasting*.

Appendix

Objective Verification Results Listed as a Function of Height

As specified in the original evaluation protocol and described in section 3.2, objective verification results are listed as a function of geopotential height. During the pre-final report discussions, it was stated that wind variables are of primary interest for applications to shuttle flight rules and should be listed in tabular format for direct reference. Plots of wind speed and direction errors as a function of height (not shown) exhibit exactly the same characteristics as those shown in Figs. 4.18 through 4.21. Therefore, the discussions in sections 4.2.4 and 4.2.5 are applicable to the wind speed and direction errors listed below. Although results for u and v wind components are not discussed in previous sections they are generally consistent with results for wind speed. As discussed in section 4, substantial differences do not appear to exist between the 0300 and 1500 UTC forecast cycles. Moreover, the statistics do not reveal any obvious differences when the results are stratified by the 950- to 600-mb layer-averaged wind direction. For these reasons, all available data from each season and verification period (see section 3.2 and Fig. 3.1) are included in the statistical calculations below. Results from TBW are not shown but are in fact very similar to those shown below for XMR. Standard deviations are not shown because they can be calculated from the bias and RMS errors using Eq. 4 and because they were not requested in the original evaluation protocol. Sample sizes collected at XMR and EDW are listed in Table A.9 as a function of height for each season. At EDW, results below 3000 ft are not available since the lowest level of data extracted from model point forecasts at that location is at an elevation of 3238 ft.

Table A.1. Warm season biases for wind variables at XMR as a function of geopotential height (kft). See Fig. 3.1 for definitions of verification periods 1, 2, and 3.

	U-wind (m s^{-1})			V-wind (m s^{-1})			Wind Speed (m s^{-1})			Wind Direction (°)		
Verf. Period Height (kft):	1	2	3	1	2	3	1	2	3	1	2	3
1	-0.1	0.1	0.0	-0.5	-0.6	0.4	-0.1	-0.2	0.2	-11	-8	-3
2	-0.8	-0.2	-0.2	0.3	-0.5	1.1	0.2	0.2	0.7	-8	-3	-5
3	-1.4	-0.5	-0.8	0.2	0.1	1.1	0.6	0.2	0.8	-2	1	-5
5	-2.0	-0.6	-0.9	0.6	0.4	1.2	0.5	0.0	0.2	-1	-12	-13
10	-0.8	0.0	0.2	-0.3	-0.4	-0.6	0.2	0.0	0.4	-1	-7	-1
12	-0.7	-0.1	0.2	-0.4	-0.4	-0.4	-0.1	-0.1	0.0	2	-2	-4
20	-1.3	-0.5	-0.6	-0.7	-0.1	0.5	-0.1	-0.1	0.1	0	1	0
25	-0.8	-0.5	-0.5	-0.4	-0.2	-0.2	0.4	-0.3	0.1	-7	0	-4
28	-0.3	-0.1	0.0	-0.4	-0.2	0.0	0.7	-0.2	0.2	1	-1	-6
35	1.4	1.1	1.3	0.3	-0.8	-0.6	0.8	0.3	0.6	-1	1	-9
38	1.4	1.4	1.8	0.8	-1.0	-0.2	0.6	0.4	0.5	-2	2	-7
45	3.1	2.1	1.9	1.3	-1.4	0.5	1.7	1.8	1.0	-9	2	-9
50	3.9	1.3	1.6	-0.3	0.2	-0.4	2.0	1.0	0.9	-11	-3	-10
55	4.5	1.4	3.1	0.5	1.0	-0.8	1.0	-0.2	1.4	-15	0	-11
60	5.4	3.5	4.1	2.0	2.0	-0.1	-2.4	-1.7	-1.4	9	9	-5
70	9.0	7.8	8.2	7.6	2.7	3.3	-3.0	-5.0	-5.2	59	28	34

Table A.2. Cool season biases for wind variables at XMR as a function of geopotential height (kft). See Fig. 3.1 for definitions of verification periods 1, 2, and 3.

	U-wind (m s^{-1})			V-wind (m s^{-1})			Wind Speed (m s^{-1})			Wind Direction (°)		
Verf. Period Height (kft):	1	2	3	1	2	3	1	2	3	1	2	3
1	-0.2	0.1	-0.3	-0.8	-0.7	0.1	0.3	0.4	0.8	0	-5	-2
2	-0.9	-0.6	-0.7	-0.6	-0.6	0.2	0.9	0.8	1.2	2	-2	0
3	-1.3	-0.6	-0.8	0.1	0.1	0.8	0.5	0.3	1.0	2	9	7
5	-1.1	-0.8	-0.4	1.1	0.1	0.9	-0.5	-0.3	0.5	-2	-3	5
10	-0.8	-0.4	-0.8	0.0	0.1	-0.4	-0.8	0.0	-0.3	1	5	0
12	-1.0	-0.7	-0.9	0.0	0.2	-0.6	-0.7	-0.1	-0.4	5	0	3
20	-1.0	-1.3	-0.9	0.1	0.1	-0.2	-0.5	-0.9	-0.7	-1	0	4
25	-0.4	-0.6	-0.2	-0.1	0.1	0.5	-0.2	-0.3	0.0	1	-1	2
28	-0.3	-0.1	-0.5	-0.3	-0.1	0.7	-0.2	0.0	-0.5	1	0	2
35	0.6	0.7	0.7	-0.6	0.0	0.3	0.5	0.3	0.5	1	0	1
38	0.7	0.7	0.8	0.1	-0.9	-0.3	0.8	0.1	0.5	-2	1	0
45	1.0	1.2	0.9	0.2	-0.2	-0.6	1.5	1.5	1.7	-1	0	1
50	1.9	0.9	0.7	-0.2	0.5	-0.3	1.4	1.1	0.8	0	0	1
55	3.0	0.2	2.2	-1.1	1.0	-0.4	3.0	0.6	2.1	1	-2	-2
60	6.8	4.9	6.4	-0.8	1.1	-0.2	5.9	4.3	5.7	-1	-9	-5
70	10.3	10.1	8.1	3.2	0.2	1.4	7.6	8.1	6.4	8	-6	-6

Table A.3. Warm season RMS errors for wind variables at XMR as a function of geopotential height (kft). See Fig. 3.1 for definitions of verification periods 1, 2, and 3.

	U-wind (m s^{-1})			V-wind (m s^{-1})			Wind Speed (m s^{-1})			Wind Direction (º)		
Verf. Period Height (kft):	1	2	3	1	2	3	1	2	3	1	2	3
1	2.2	2.2	2.7	2.4	2.7	3.0	1.9	2.2	2.7	51	52	50
2	2.3	1.9	2.6	2.2	2.6	3.1	2.0	2.0	2.9	45	49	52
3	2.4	1.9	2.8	2.3	2.5	3.0	2.1	1.8	2.9	47	57	55
5	3.0	2.4	2.8	2.5	2.8	2.9	2.6	2.2	3.0	52	55	63
10	2.5	2.4	2.8	2.4	2.5	3.0	2.5	2.3	2.9	49	48	48
12	2.3	2.4	2.8	2.2	2.7	3.0	2.1	2.5	3.0	47	47	54
20	2.3	2.4	2.8	2.3	2.3	2.5	2.1	2.0	2.3	49	53	50
25	2.5	2.6	3.2	2.7	2.6	2.5	2.5	2.6	2.8	44	43	50
28	2.8	2.6	3.6	3.1	3.1	3.2	3.0	2.7	3.2	39	40	47
35	3.9	4.5	5.0	3.7	4.2	5.1	3.6	4.2	4.8	42	43	49
38	4.3	4.7	5.7	3.5	4.9	5.1	4.0	4.2	5.1	36	42	49
45	5.7	4.6	4.6	4.9	4.9	4.9	5.0	4.5	4.5	42	36	37
50	5.7	4.1	3.8	3.7	3.7	3.7	4.9	3.8	3.3	43	47	43
55	5.5	3.3	4.0	3.6	3.6	2.8	3.9	3.1	3.2	60	51	48
60	5.9	4.0	4.8	3.4	3.3	2.5	4.3	3.4	3.3	76	58	62
70	9.6	8.4	8.8	8.2	4.1	4.6	5.4	6.4	7.0	85	78	80

Table A.4. Cool season RMS errors for wind variables at XMR as a function of geopotential height (kft). See Fig. 3.1 for definitions of verification periods 1, 2, and 3.

	U-wind (m s^{-1})			V-wind (m s^{-1})			Wind Speed (m s^{-1})			Wind Direction (º)		
Verf. Period Height (kft):	1	2	3	1	2	3	1	2	3	1	2	3
1	2.1	2.3	2.5	2.5	2.8	2.7	2.1	2.2	2.2	30	39	35
2	2.1	2.1	2.5	2.5	2.8	3.0	2.3	2.1	2.6	37	39	39
3	2.4	2.4	2.9	2.6	2.4	2.9	2.2	2.1	2.8	40	46	40
5	2.7	2.8	3.2	3.0	2.9	3.3	2.5	2.6	3.1	36	43	46
10	2.1	2.2	2.7	2.2	2.8	3.0	2.0	2.1	2.8	38	48	46
12	2.1	2.6	2.7	2.0	2.7	3.0	2.0	2.1	2.6	37	37	45
20	2.4	3.1	3.2	2.6	2.4	2.9	2.5	3.0	3.0	19	19	28
25	2.8	3.0	3.5	2.9	3.4	3.7	2.6	3.1	3.1	14	15	22
28	3.1	2.9	3.4	3.2	3.3	3.4	2.9	3.4	3.4	15	13	19
35	3.6	4.4	4.9	4.1	4.3	5.3	3.4	4.5	4.5	11	13	16
38	3.7	4.0	4.6	4.6	4.1	4.6	3.8	3.8	4.4	13	13	17
45	4.5	4.3	4.3	5.1	4.4	4.6	4.4	4.5	4.9	12	9	9
50	4.8	4.2	4.6	4.7	4.3	4.9	4.2	4.3	4.7	12	11	12
55	4.7	3.4	4.2	3.3	4.2	3.5	4.6	3.5	4.4	15	18	14
60	7.6	5.9	7.2	3.3	3.3	3.6	6.9	5.6	6.7	37	37	37
70	10.8	10.5	8.7	4.4	3.6	4.5	8.9	9.4	8.0	72	65	66

Table A.5. Warm season biases for wind variables at EDW as a function of geopotential height (kft). See Fig. 3.1 for definitions of verification periods 1, 2, and 3.

	U-wind (m s^{-1})			V-wind (m s^{-1})			Wind Speed (m s^{-1})			Wind Direction (°)		
Verf. Period Height (kft):	1	2	3	1	2	3	1	2	3	1	2	3
1	---	---	---	---	---	---	---	---	---	---	---	---
2	---	---	---	---	---	---	---	---	---	---	---	---
3	---	---	---	---	---	---	---	---	---	---	---	---
5	-0.6	0.3	-1.0	-0.9	-1.4	-1.6	-1.5	-0.3	-1.2	-6	4	7
10	-0.6	0.0	-0.5	1.2	-0.4	0.7	-1.0	-1.2	-1.4	-11	-13	-15
12	-0.8	-0.3	-0.7	1.1	-0.2	0.8	-0.5	-0.9	-0.8	-20	-11	-18
20	-0.9	-1.2	-2.1	1.0	0.8	0.5	0.1	-0.2	0.1	-11	-9	-14
25	-0.9	-1.8	-1.6	0.9	1.0	1.1	-0.5	-0.9	-1.1	-11	-8	-15
28	-1.2	-1.5	-1.9	1.2	1.4	1.2	-0.2	-0.7	-1.4	-7	-7	-12
35	-0.1	-0.6	-1.2	0.5	1.4	1.2	0.1	-0.3	-1.0	-1	-7	-8
38	0.2	-0.6	-1.3	0.6	0.6	0.1	0.3	0.3	-1.1	-1	-2	-2
45	-0.8	-0.4	-1.0	0.6	0.7	0.0	-0.5	-1.0	-1.5	-3	0	2
50	-0.5	-0.5	-0.5	1.0	0.2	0.6	-0.8	-0.5	-0.3	2	1	2
55	1.3	1.5	2.2	1.3	-0.9	0.7	0.2	0.1	1.0	4	1	-1
60	2.5	2.7	3.6	-0.3	-2.0	0.3	-1.3	0.0	0.6	13	5	13
70	5.9	3.7	5.2	-0.5	-0.9	-0.1	-2.1	-1.2	-1.8	11	-2	26

Table A.6. Cool season biases for wind variables at EDW as a function of geopotential height (kft). See Fig. 3.1 for definitions of verification periods 1, 2, and 3.

	U-wind (m s^{-1})			V-wind (m s^{-1})			Wind Speed (m s^{-1})			Wind Direction (°)		
Verf. Period Height (kft):	1	2	3	1	2	3	1	2	3	1	2	3
1	---	---	---	---	---	---	---	---	---	---	---	---
2	---	---	---	---	---	---	---	---	---	---	---	---
3	---	---	---	---	---	---	---	---	---	---	---	---
5	-1.4	-2.5	-3.6	-0.1	-0.2	-0.3	-0.2	-0.4	0.1	-8	3	5
10	-1.1	-2.7	-3.0	0.9	0.7	0.4	-0.6	-0.6	-1.2	-7	-2	-1
12	-1.2	-1.9	-2.4	1.1	0.5	1.0	-0.6	-0.6	-1.6	2	5	4
20	0.9	0.9	-0.6	0.8	1.3	1.9	0.6	-0.3	-1.2	-6	-9	-10
25	-0.1	0.1	-0.6	1.1	1.8	2.5	-1.0	-0.5	-2.0	-11	-10	-9
28	-0.2	1.0	0.3	1.2	1.2	2.1	0.2	0.6	-0.2	-6	-6	-6
35	1.7	2.4	1.4	0.9	2.8	4.4	0.6	-0.2	-1.5	-6	-6	-9
38	0.0	0.7	1.0	0.2	1.3	2.9	-1.5	-0.7	-2.0	-2	-5	-8
45	1.5	2.5	2.2	-2.6	0.5	0.5	2.1	1.2	1.2	5	-3	-3
50	-0.5	1.7	1.6	1.3	3.1	1.7	-1.3	0.4	0.4	-3	-8	-5
55	0.9	1.7	2.7	0.8	0.8	2.0	0.4	1.2	2.1	-7	-5	-5
60	1.2	3.4	4.9	-0.4	0.6	1.8	1.3	2.5	3.9	-1	-3	-10
70	4.1	5.4	4.7	-2.4	-1.9	-3.1	4.7	5.4	3.9	-2	7	-3

Table A.7. Warm season RMS errors for wind variables at EDW as a function of geopotential height (kft). See Fig. 3.1 for definitions of verification periods 1, 2, and 3.

	U-wind (m s^{-1})			V-wind (m s^{-1})			Wind Speed (m s^{-1})			Wind Direction (º)		
Verf. Period Height (kft):	1	2	3	1	2	3	1	2	3	1	2	3
1	---	---	---	---	---	---	---	---	---	---	---	---
2	---	---	---	---	---	---	---	---	---	---	---	---
3	---	---	---	---	---	---	---	---	---	---	---	---
5	4.0	4.2	3.6	2.6	2.7	3.4	3.7	3.7	3.7	35	42	36
10	2.6	3.1	3.2	2.4	2.9	3.4	2.4	2.9	3.4	38	48	44
12	2.6	3.3	3.5	2.7	3.0	3.3	2.2	3.0	3.7	37	42	41
20	2.9	3.2	4.4	3.1	3.6	3.9	2.9	3.3	3.6	27	32	42
25	3.1	4.1	4.7	3.3	3.0	3.6	3.2	3.4	4.6	28	30	36
28	2.9	3.4	4.4	3.4	3.9	4.1	2.6	3.1	4.2	19	26	35
35	3.4	3.7	4.2	3.4	4.2	4.6	3.6	3.4	3.9	14	24	26
38	3.4	4.0	4.3	3.3	3.6	4.8	3.4	3.9	4.1	15	18	21
45	3.6	3.4	4.8	4.6	4.0	4.2	4.1	3.8	4.6	20	19	22
50	3.2	3.9	4.6	4.1	3.7	4.5	3.9	4.0	4.5	28	19	29
55	3.1	3.6	4.3	4.0	3.4	3.1	2.9	3.4	3.9	43	35	29
60	4.1	4.5	5.0	3.2	3.6	3.3	3.1	3.4	4.1	54	54	58
70	6.5	4.7	5.9	3.4	3.1	2.3	5.7	4.0	4.5	61	56	57

Table A.8. Cool season RMS errors for wind variables at EDW as a function of geopotential height (kft). See Fig. 3.1 for definitions of verification periods 1, 2, and 3.

	U-wind (m s^{-1})			V-wind (m s^{-1})			Wind Speed (m s^{-1})			Wind Direction (º)		
Verf. Period Height (kft):	1	2	3	1	2	3	1	2	3	1	2	3
1	---	---	---	---	---	---	---	---	---	---	---	---
2	---	---	---	---	---	---	---	---	---	---	---	---
3	---	---	---	---	---	---	---	---	---	---	---	---
5	3.8	4.6	5.2	3.4	3.3	3.6	2.8	3.7	3.6	53	60	62
10	2.4	3.8	4.2	3.3	3.6	3.4	2.8	3.2	3.7	28	31	44
12	3.1	3.5	4.4	4.0	4.3	4.1	3.1	3.5	4.2	29	32	38
20	4.1	4.5	4.3	4.0	5.8	5.6	3.5	5.5	5.3	20	28	27
25	4.9	5.6	6.0	4.4	5.3	5.9	4.3	4.7	5.9	30	24	25
28	5.0	4.9	5.3	5.0	5.4	5.9	4.5	5.0	4.7	15	19	18
35	5.2	5.9	6.1	5.2	6.6	8.1	4.8	5.2	6.2	13	14	17
38	5.2	5.5	6.4	6.3	5.9	7.5	6.2	6.0	6.8	15	17	19
45	6.0	5.8	6.0	5.7	5.7	4.9	5.8	5.1	5.1	19	20	21
50	4.2	4.0	3.6	5.1	5.6	5.2	4.7	3.9	3.7	18	19	22
55	3.5	3.4	4.2	4.3	4.4	4.6	4.0	3.7	4.3	20	18	27
60	4.7	5.9	6.8	3.4	3.6	3.6	5.2	5.2	5.8	19	20	22
70	5.8	6.8	5.4	3.7	4.2	4.7	6.8	6.8	5.5	34	26	36

Table A.9. Sample sizes of wind data used to calculate bias and RMS errors at XMR and EDW during the warm and cool seasons as a function of geopotential height (kft). See Fig. 3.1 for definitions of verification periods 1, 2, and 3.

	XMR (warm)			XMR (cool)			EDW (warm)			EDW (cool)		
Verf. Period Height (kft):	1	2	3	1	2	3	1	2	3	1	2	3
1	131	127	127	125	124	130	---	---	---	---	---	---
2	133	127	128	121	124	130	---	---	---	---	---	---
3	134	130	131	121	124	129	---	---	---	---	---	---
5	135	132	128	128	125	130	78	76	75	57	58	57
10	136	132	134	126	125	126	78	76	76	55	57	55
12	133	133	131	125	128	128	78	74	74	56	53	55
20	133	134	126	126	126	129	73	74	73	56	56	56
25	134	132	131	127	128	129	72	71	72	55	58	55
28	133	131	131	127	125	129	74	70	72	55	55	53
35	136	134	130	128	127	130	72	72	72	51	55	53
38	136	131	129	124	126	128	72	69	73	54	57	54
45	132	132	128	125	128	126	71	70	72	53	55	52
50	136	134	124	122	122	127	65	70	70	53	54	53
55	120	115	109	98	90	94	58	60	61	40	44	42
60	120	113	112	93	90	93	60	61	58	40	42	42
70	117	111	106	92	86	87	37	37	37	26	26	26